UNCLASSIFIED

DEFENCE RESEARCH ESTABLISHMENT
CENTRE DE RECHERCHES POUR LA DÉFENSE
VALCARTIER, QUÉBEC

DREV - TR - 2000-156
Unlimited Distribution / Distribution illimitée

PASSIVE STANDOFF DETECTION OF CHEMICAL VAPORS BY DIFFERENTIAL FTIR RADIOMETRY

by

Jean-Marc Thériault

January / janvier 2001

Approved by / approuvé par

Section Head / Chef de section

8 Jan 2001
Date

SANS CLASSIFICATION

ABSTRACT

This report presents a novel method for the passive standoff detection of chemical vapors by differential radiometry. The originality of the method lies on the use of a double-input beam Fourier Transform Infrared (FTIR) interferometer optimized for optical subtraction. For implementing this method, a radiative transfer model is formulated for the general case of slant path scenarios containing any type of background scenes. A procedure of radiometric calibration adapted for differential detection with a double-input beam FTIR interferometer is developed. A detection algorithm (GASEM) that controls the interferometer data acquisition and performs the on-line monitoring of chemical vapor parameters is described and validated. The differential detection method has been successfully tested in the field on several chemical vapors. In particular, it has been used to map the integrated concentration and the temperature of a plume of methanol vapor. In this case, the uncertainties on the methanol plume measurements have been estimated to be of the order of 15 to 30% for concentration, and 2 to 5° for temperature which represents an acceptable result for this type of passive sensing.

RÉSUMÉ

Ce rapport présente une nouvelle méthode pour la détection en retrait de vapeurs chimiques par radiométrie différentielle infrarouge. L'originalité de cette méthode repose sur l'utilisation d'un interféromètre infrarouge à transformation de Fourier (FTIR) à double entrée optimisé pour la soustraction optique. En vue de sa mise en oeuvre, nous avons formulé un modèle de transfert radiatif pour le cas général de parcours obliques faisant intervenir différents types d'arrière-plans. Nous avons ensuite élaboré une procédure d'étalonnage radiométrique adaptée à la détection différentielle pour l'interféromètre FTIR à double entrée. Nous décrivons et vérifions aussi un algorithme de détection (GASEM) qui contrôle la cueillette des données par l'interféromètre et le monitorage des paramètres de la vapeur chimique. La méthode de détection différentielle a été testée sur le terrain avec succès sur plusieurs vapeurs chimiques: en particulier, on l'a utilisée pour cartographier la concentration intégrée et la température d'un nuage de vapeur de méthanol. Dans ce cas nous estimons que les incertitudes sur les paramètres du nuage de méthanol varient de 15 à 30% sur la concentration et de 2 à 5° sur la température, ce qui représente un résultat acceptable pour ce type de sondage passif.

WARNING NOTICE

The information contained herein is proprietary to Her Majesty and is provided to the recipient on the understanding that it will be used for information and evaluation purposes only. Any commercial use, including use for manufacture, is prohibited. Release to third parties of this publication or of information contained herein is prohibited without the prior written consent of DND Canada.

© Her Majesty the Queen in Right of Canada as represented by the Minister of National Defence, 2001

TABLE OF CONTENTS

ABSTRACT / RÉSUMÉ i

EXECUTIVE SUMMARY v

1.0 INTRODUCTION 1

2.0 DIFFERENTIAL DETECTION METHOD 2

2.1 Theory for Differential Detection 2
2.2 Background Variability Considerations 7

3.0 EXPERIMENTAL ASPECTS OF THE DIFFERENTIAL DETECTION 13

3.1 Description of the CATSI Instrument 14
3.2 Equations for the Radiometric Calibration 16
3.3 Procedure for the Radiometric Calibration 20
3.4 Advantages of the Double-Beam Interferometer for Differential Detection 25

4.0 MODELING AND ALGORITHM DEVELOPMENT 28

4.1 Minimization by SIMPLEX 29
4.2 Input and Retrieved Parameters 33
4.3 Atmospheric Transmission and Emission Modeling 38
4.4 Background Drifts Modeling 42
4.5 Correlation Factor 46
4.6 Algorithm Functionalities and Examples of Operation 50

5.0 REMOTE MONITORING OF CHEMICAL VAPORS: RESULTS 56

5.1 Methanol Vapor Releases and Monitoring Conditions 56
5.2 Quantization Results for Methanol 61
5.3 Ammonia and Mixtures of Ammonia-Methanol 66

6.0 SUMMARY AND CONCLUSIONS 66

7.0 ACKNOWLEDGMENTS 71

8.0 REFERENCES 72

FIGURES 1 to 24

EXECUTIVE SUMMARY

The Canadian Forces are using a variety of electro-optical systems for the remote sensing of target characteristics. In the past few years, the development of passive IR spectral sensors has grown to a point at which it is now considered a vital technology for the remote monitoring of battlefield environment, providing unique information on the ongoing maneuvers. One of the most promising applications in passive spectral surveillance is the remote detection and identification of toxic vapors. There is a growing need for fieldable, rapid-response surveillance systems for providing timely and accurate chemical threat assessments, thus ensuring prompt avoidance and deployment of countermeasures.

Defence Research Establishment Valcartier (DREV) is currently developing a passive Fourier Transform InfraRed (FTIR) technique for the standoff detection and identification of chemical vapors. A well-known difficulty associated with this technique is that the recorded signal also contains a large amount of unwanted background radiation. This background radiation often exceeds the target radiation by more than two orders of magnitude. Consequently, the selected processing method must be highly efficient in filtering the background content in addition to its capability for target pattern recognition. Existing methods have strengths and weaknesses, depending on the scenario under consideration. For instance, certain methods are efficient for down-looking surveillance scenarios involving graybody-type backgrounds but are very limited for up-looking scenarios involving sky-type backgrounds. In some other methods, the need for approximations definitely restricts their use to a narrow class of applications. It can be stated that in many existing methods the approach used for removing, filtering or suppressing the background component is not robust enough to support a wide variety of surveillance scenarios.

This report presents a novel approach for the passive standoff detection of chemical vapors by differential FTIR radiometry. This differential method has a unique advantage with regard to background removal, i.e. its efficiency is approximately insensitive to the background type. The method is based on the use of a double-input beam FTIR interferometer where one input points at the background-scene and the other aims at the target-scene. With this configuration, the two probed scenes are optically subtracted in real-time yielding a cloud vapor spectrum minimally perturbed by the background radiation. The research effort has been concentrated in developing a radiative transfer model and a detection algorithm (GASEM) for the general case of slant path scenarios containing any type of background scenes. This development has highlighted several attributes that make the differential detection method particularly efficient. The greatest advantage found with the proposed approach is to provide, in the field, a spectrally clean signature of the remote chemical plume which facilitates its processing in real-time. The method has been successfully used for the on-line monitoring of several compounds. For instance, it has been utilized to map the integrated concentration and the temperature of a plume of methanol vapor that acts as a generic simulant for chemical agents. The uncertainties on the methanol plume monitoring have been estimated to be of the order of 15-30% for the integrated concentration, and 2 to 5° for the temperature. This level of accuracy is quite acceptable for this type of passive sounding.

The results of this work may also have a significant impact on several other remote sensing applications involving atmospheric pollution monitoring from the ground or from an airborne platform. In addition, this work contributes directly to Canadian inputs to TTCP CBD AG-46, TTCP SEN AG-4 and NATO TG-16 international technical groups.

1.0 INTRODUCTION

There exists a variety of electro-optical (EO) sensors being developed to assist the Canadian Forces in surveillance operations. Among them, passive IR spectral sensors are becoming a vital technology for the remote sensing of battlefield environment that can provide unique information on ongoing maneuvers. One of the most promising military applications in passive spectral surveillance is the remote detection and identification of toxic vapors. The proliferation of chemical weapons continues to be a serious threat to world security. There is a growing need for fieldable, rapid-response surveillance systems for providing timely and accurate chemical threat assessments, thus ensuring prompt avoidance and deployment of countermeasures.

A well-known difficulty associated with the passive standoff detection and identification of chemical vapors is that the recorded signal also contains a large amount of unwanted background radiation. This background radiation often exceeds the target one by more than two orders of magnitude. Consequently, the selected processing technique must be highly efficient in filtering the background content in addition to its capability for target pattern recognition. There exists a variety of signal processing techniques developed for the passive standoff detection of chemical vapors. Several of these techniques have been reviewed or described in recent papers (Refs. 1-3). These techniques are usually designed for a specific class of detection scenarios. For instance, some processing algorithms are very efficient for down-looking surveillance scenarios (Ref. 1) involving graybody-type backgrounds but are not optimized for up-looking scenarios involving sky-type backgrounds. In some other cases, the opposite is true (Ref. 2). This limitation is due to the fact that the approach used for removing, filtering or suppressing the background component is not flexible enough to support a wide variety of surveillance scenarios.

Defence Research Establishment Valcartier (DREV) is currently developing a passive FTIR radiometric technique for the standoff detection and identification of chemical agents at ranges of up to 5 km. The differential detection method we propose in this document has a unique advantage with regard to background removal in that its efficiency is approximately insensitive to background type. The method is based on the use of a specialized double-input beam FTIR interferometer (Refs. 4, 5) where one input points at the background-scene and the other, at the target-scene. With this configuration, the two probed scenes are optically

combined into a single detector resulting in a real-time optical subtraction. This yields a cloud vapor spectrum minimally perturbed by the background radiation.

In this report we describe and analyze the DREV differential method proposed for the passive standoff detection of chemical vapors. In Chapter 2, we first describe the radiative transfer model that supports the method for the general case of slant path scenarios containing any type of background scenes. The general procedure of radiometric calibration adapted for differential detection with a double-input beam FTIR interferometer is presented in Chapter 3. In Chapter 4, a detailed description of the GASEM processing algorithm developed for the on-line remote monitoring of chemical vapors is given together with several examples of its capabilities. In Chapter 5, typical field monitoring results obtained on different chemical vapors are presented and discussed as a verification of the method. Finally, Chapter 6 summarizes the work and draws conclusions on the performance of the proposed approach.

This work was performed at DREV between September 1998 and April 2000 under Thrust 2d - Land Forces Tactical Surveillance and Counter-Surveillance, Work Unit 2km10: Gaseous Emission Monitoring for Surveillance: Feasibility Study.

2.0 DIFFERENTIAL DETECTION METHOD

2.1 Theory for Differential Detection

In the following, the equations of the method are developed in relation with the atmospheric layering depicted in Fig. 1. For a plane-parallel clear atmosphere (free of target gas) in local thermodynamic equilibrium with no scattering, the total path radiance L_{clear} measured at any observation angles, including both horizontal and slant path scenarios, may be expressed in terms of three components

$$L_{clear} = F_{far}\tau_{near}\tau_{air} + B_{air}(1-\tau_{air})\tau_{near} + N_{near} \qquad [1]$$

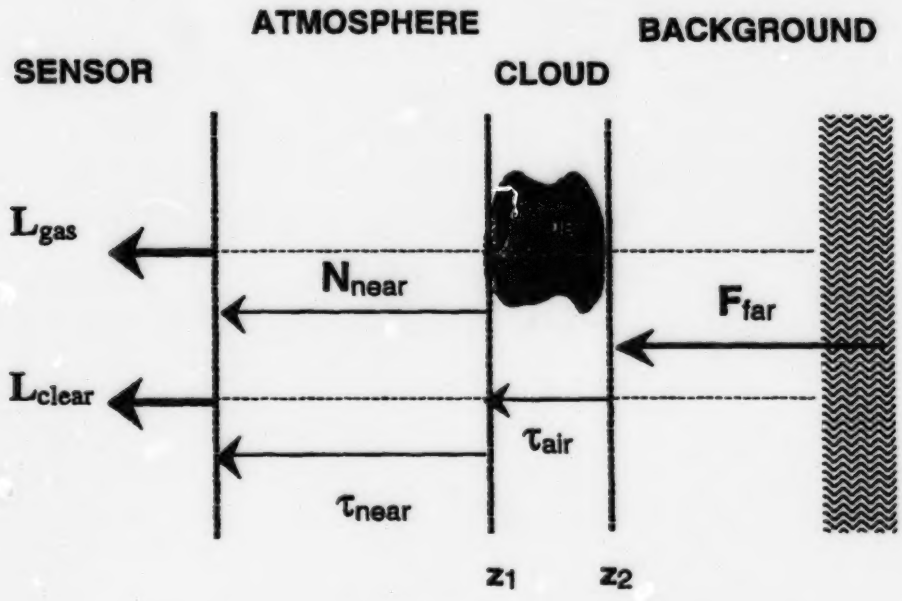

FIGURE 1 - The diagram and the associated terminology defining the 3-layer geometry for the differential detection with a dual beam interferometer

where F_{far} corresponds to the far-field radiance evaluated at position z_2, τ_{near} is the transmittance from position z_1 to the sensor, B_{air} and τ_{air} are the Planck radiance and the transmittance associated with the air layer and N_{near} corresponds to the near-field path radiance of the atmosphere from position z_1 to the sensor. Similarly, the total radiance L_{gas} of an atmosphere containing a target gas layer at position z_1 (Fig. 1) is given by

$$L_{gas} = F_{far}\tau_{near}\tau_{gas} + B_{gas}\left(1-\tau_{gas}\right)\tau_{near} + N_{near} \qquad [2]$$

where B_{gas} and τ_{gas} are the associated Plank radiance and the transmittance of the target gas layer. τ_{gas} is connected to the integrated-path concentration (CL) by the Beer-Lambert relation

$$\tau_{gas} = \exp\left(-\alpha_{\nu} CL\right) \qquad [3]$$

where α_ν is the spectrally dependent absorption coefficient (1/ppm-m), C is the volume concentration (ppm) and L (m) is the length of the target gas sample. Note that the quantity of interest, CL, is given here in ppm-m. It is important to note that the Planck radiance terms B in Eqs. 1 and 2 assume different temperatures for the target gas layer (T_{gas}) and the air layer (T_{air}).

Subtracting the atmospheric radiance of the clear atmosphere (Eq. 1) from the radiance of the gas contaminated atmosphere (Eq. 2) leads to the following expression for the radiance differential

$$\delta L_{calc} \equiv \left(L_{gas} - L_{clear}\right) = \left(\tau_{air} - \tau_{gas}\right)\left[B_{gas} - F_{far}\right]\tau_{near} + \left(1 - \tau_{air}\right)\left[B_{gas} - B_{air}\right]\tau_{near}. \qquad [4]$$

The first term on the right-hand side of the equation is the leading emission term: the radiance differential associated with the target gas is proportional to gas absorption differential times the radiative contrast between the Planck and far-field radiances. The second term can be seen as a correction when the gas temperature is different from the air temperature. Once δL is measured, τ_{gas} can be evaluated from the knowledge of B_{gas}, B_{air}, τ_{air}, τ_{near} and F_{far}. The last four terms have to be evaluated remotely because they are distant from the sensor. Except for the target gas temperature (to evaluate B_{gas}), all other quantities can be computed using a propagation model such as MODTRAN (or others) provided that the local meteorological profiles of temperature and humidity are available. These profiles can be obtained from local radiosondes or alternatively by inversion of atmospheric emission. Default atmospheres can be used for other constituent profiles. However, there is difficulty in the evaluation of the far field radiance term F_{far} which usually contains two contributions, i.e. the far-field atmospheric emission and the distant scene emission which is often quite ambiguous to evaluate: it can be mountains, forests, clouds, sea water, ground or a variety of other background types. However, from Eq. 1 $F_{far}\tau_{near}$ can be replaced in Eq. 2 to give the following general equation for the differential detection:

$$\begin{aligned}\delta L_{calc} = {} & \left(1 - \tau_{air}\right)\left[B_{gas} - B_{air}\right]\tau_{near} \\ & + \left(1 - \frac{\tau_{gas}}{\tau_{air}}\right)\left[\left(B_{gas} - B_{air}\right)\tau_{air}\tau_{near} + N_{near} + B_{air}\tau_{near} - L_{clear}\right]\end{aligned} \qquad [5]$$

where the clear atmosphere radiance L_{clear} that now appears in the equation has to be evaluated experimentally (measurement) prior to or after the differential measurement. It is important to emphasize that Eq. 5 is in principle a general equation for differential detection of any target gas at any concentration and temperature. Moreover, the parameters to be computed with a propagation model, i.e. B_{air}, τ_{air}, τ_{near} and N_{near} that are known as near field terms, require only near field meteorological profiles (nothing beyond the target gas layer). This is highly suitable in practice because the accuracy of meteorological profiles obtained by guessing or more precisely by remote sensing usually decreases with distance.

Equation 5 can be simplified to accommodate different scenarios. For instance, a first simplification occurs by assuming that the thickness of the thin air layer (or gas layer) is negligible compared to the total path from the gas to the sensor. In this case, $\tau_{air} = 1$ and Eq. 5 reduces to

$$\delta L_{calc} = \left(1-\tau_{gas}\right)\left[B_{gas}\tau_{near} + N_{near} - L_{clear}\right] . \qquad [6]$$

Moreover, for slant path measurements, a good approximation for the near-field emission term, N_{near}, is given by

$$N_{near} = \left(1-\tau_{near}\right)B\left(\frac{T_{air}^{0} + T_{air}^{d}}{2}\right), \qquad [7]$$

where the effective temperature for the Plank emission term (B) is taken as the average of the temperature at both end of the propagation path i.e., at zero range near the receiver (T_{air}^{0}), and at range d near the cloud vapor (T_{air}^{d}). For the horizontal path case where $T_{air} = T_{air}^{0} = T_{air}^{d}$, the atmospheric emission component reduces to

$$N_{near} = \left(1-\tau_{near}\right)B_{air} , \qquad [8]$$

which further simplifies the radiance differential to

$$\delta L_{calc} = \left(1-\tau_{gas}\right)\left[\left(B_{air} - L_{clear}\right) + \left(B_{gas} - B_{air}\right)\tau_{near}\right] . \qquad [9]$$

Equation 9 applies to horizontal path scenarios where the gas temperature is different from

the air temperature. For cases where the target gas is in thermal equilibrium with the ambient air ($B_{gas} = B_{air}$) the radiance differential simplifies to the well-known expression

$$\delta L_{calc} = \left(1 - \tau_{gas}\right)\left[B_{air} - L_{clear}\right] , \qquad [10]$$

where it is recalled that B_{air} is computed and L_{clear} is measured. It is interesting to note that in Eq. 10 the range dependence totally disappears. As seen later, Eqs. 6, 9 and 10 are useful approximations which help to understand the observed spectral signatures in many different scenarios. For instance, Figure 2 shows a typical simulation of differential detection for ammonia (100 ppm-m) where L_{gas}, L_{clear} and the resulting difference δL are compared for the horizontal path scenario. Note that for clarity, a negative offset (-2×10^{-7}) has been added to the L_{gas} curve. For this case the temperature of ammonia vapor was five degrees lower that the apparent background temperature yielding absorption features in δL (negative modulations). When the ammonia is at a higher temperature than the background, emission features are observed (positive modulations).

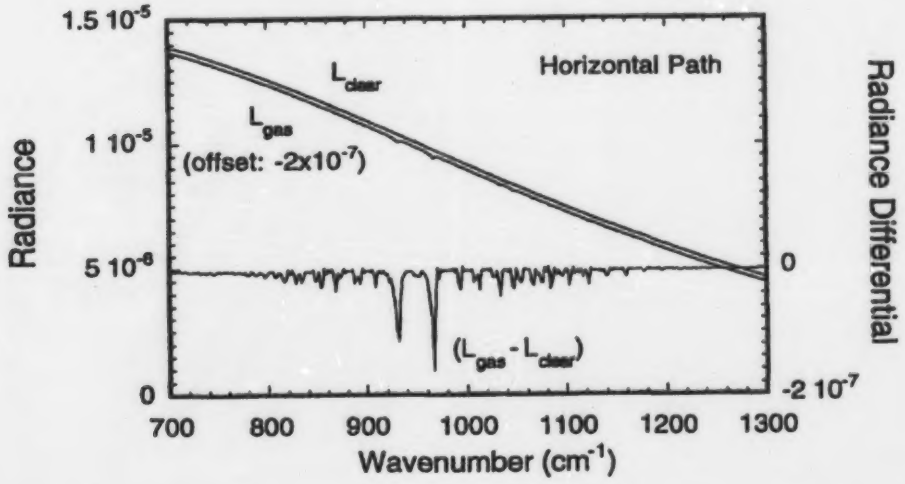

FIGURE 2 -Simulation of differential detection of ammonia (100 ppm-m) for the horizontal path scenario (see text)

P515096.PDF [Page: 15 of 86]

2.2 Background Variability Considerations

The main purpose of adopting a differential approach for the detection of chemical vapors can been understood from application of the previous equations. For that we can rewrite Eq. 2 in the following form

$$L_{gas} = \left(N_{near} + F_{far}\tau_{near}\right) + \left(1-\tau_{gas}\right)\left[B_{gas} - F_{far}\right]\tau_{near} \ , \qquad [11]$$

and compared it with the radiance differential establish at Eq. 4 in the limit of a thin air layer ($\tau_{air} = 1$)

$$\delta L = \left(1-\tau_{gas}\right)\left[B_{gas} - F_{far}\right]\tau_{near}. \qquad [12]$$

It can be seen from Eq. 11 that in direct detection mode, the small signal from the cloud vapor $\left[\left(1-\tau_{gas}\right)\left(B_{gas} - F_{far}\right)\right]\tau_{near}$ is imbedded in two strong signals (N_{near} and $F_{far}\tau_{near}$). The sum of these two strong signals actually represents the clear-scene radiance (L_{clear}). Thus in the direct detection mode where only the target scene radiance (L_{gas}) is probed, very efficient methods must be applied to filter out or to estimate the two undesired contributions (N_{near} and $F_{far}\tau_{near}$). Errors of only a few percents in evaluating these contributions yield atmospheric lines residuals which can dramatically interfere with the true vapor spectrum and thus create false alarms. In differential detection mode these undesired contributions are removed prior to applying the detection algorithm which should result in a more reliable method. However, to establish Eqs. 4 or 12 we have assumed that the far-field background radiance (F_{far}) is the same for both L_{clear} and L_{gas} measurements. In practice this is not always the case due to temporal and spatial variations encountered in natural backgrounds such as terrains, forests, mountains, clouds and others. This issue of background variability is addressed below.

There exist several methods to perform differential detection with both single-beam and double-beam instruments. They can be divided into two groups, i.e. sequential acquisition and simultaneous acquisition approaches. For the sequential acquisition approach, the two spectra are acquired in two steps: First, a clear-scene measurement (L_{clear}), and second, a target-scene measurement. Since the clear-scene acquisition is not performed at the same time as the target measurement, the subtraction of the two can produce errors especially when

applied to rapidly moving backgrounds. The sequential acquisition approach is generally associated with single-beam instruments having a single-pixel detector.

In the simultaneous acquisition approach, a clear-scene radiance is acquired at the same time as the target-scene measurement. Simultaneous acquisitions can be done with a single-beam instrument having a focal plane array where the scenes subtraction can be performed electronically from selected pixels. Simultaneous subtraction can also be done optically by using a double-input beam interferometer such as described in the next chapter. In this case the clear-scene and the target-scene radiances are optically combined into a single detector resulting in a real-time subtraction.

In the following, a set of equations is derived to evaluate the impact of background variations in differential detection for both the sequential and the simultaneous subtraction approaches. Figure 3 provides a schematic view for comparing the different cases treated: Figs. 3a, 3c and 3e are associated with the sequential acquisition approach, and Figs. 3b, 3d and 3f are associated with the simultaneous subtraction approach.

2.2.1 Sequential Versus Simultaneous Acquisition with Constant Background

Referring to the ideal case of no background drift (Eqs. 1, 2 and 6) and assuming a τ_{air}= 1 for the thin air layer we have for the recorded L_{gas} and the reference clear scene radiance L'_{clear},

$$L'_{clear} = F_{far}\tau_{near}\tau_{air} + N_{near} \qquad [13a]$$

$$L_{gas} = F_{far}\tau_{near}\tau_{gas} + B_{gas}\left(1-\tau_{gas}\right)\tau_{near} + N_{near} \qquad [13b]$$

yielding the resulting difference

$$\delta L = \left(L_{gas} - L'_{clear}\right) = \left(1-\tau_{gas}\right)\left[B_{gas}\tau_{near} + N_{near} - L'_{clear}\right] \qquad [13c]$$

Figures 3a and 3b compare the measurement protocols for sequential and simultaneous acquisitions, respectively. For the sequential acquisition (Fig. 3a), first the reference clear-scene radiance (L'_{clear}) is recorded and second the target-scene radiance (L_{gas}) is acquired. Note that in the sequential acquisition approach the same (L'_{clear}) is used to evaluate the

background radiance (on the right-hand side of Eq. 13c) which serves to scale the target gas emission, and to evaluate the radiance differential $\delta L = L_{gas} - L'_{clear}$ (left-hand side of Eq. 13c). For the simultaneous acquisition (Fig. 3b), first the reference clear-scene radiance (L'_{clear}) is recorded and second the radiance differential δL is directly measured. For this ideal case of a constant background such as in Figs. 3a and 3b, both approaches (sequential and simultaneous) yield the same radiance differential given by Eq. 13c.

2.2.2 Sequential Acquisition with Background Variation

To evaluate the impact of a background variation (ΔF) in the sequential acquisition approach (Fig. 3c) we write

$$L'_{clear} = F_{far}\tau_{near}\tau_{air} + N_{near} \qquad [14a]$$

$$L'_{gas} = \left(F_{far} + \Delta F\right)\tau_{near}\tau_{gas} + B_{gas}\left(1-\tau_{gas}\right)\tau_{near} + N_{near} \qquad [14b]$$

yielding

$$\delta L_{seq} = \left(L'_{gas} - L'_{clear}\right) = \Delta L_{clear}\tau_{gas} + \left(1-\tau_{gas}\right)\left[B_{gas}\tau_{near} + N_{near} - L'_{clear}\right], \qquad [14c]$$

where $\Delta L_{clear} = \Delta F\tau_{near}$ assuming that the clear-scene radiance variation is entirely due to a variation of the far-field background radiance. The superscript (")associated with L'_{gas} and L'_{clear} (below) is introduced to express the modification caused by the background variation ΔF. For the sequential acquisition approach the background variation introduces an additive term in the radiance differential (Eq. 14c) which is proportional to the clear-scene radiance variation times the transmittance of the target gas. In this case, the radiance differential is quite sensitive to background variations especially at low concentration when τ_{gas} is near unity. This means that a frequent updating of L'_{clear} would be required to minimize the impact of the background drift ΔL_{clear} on the radiance differential.

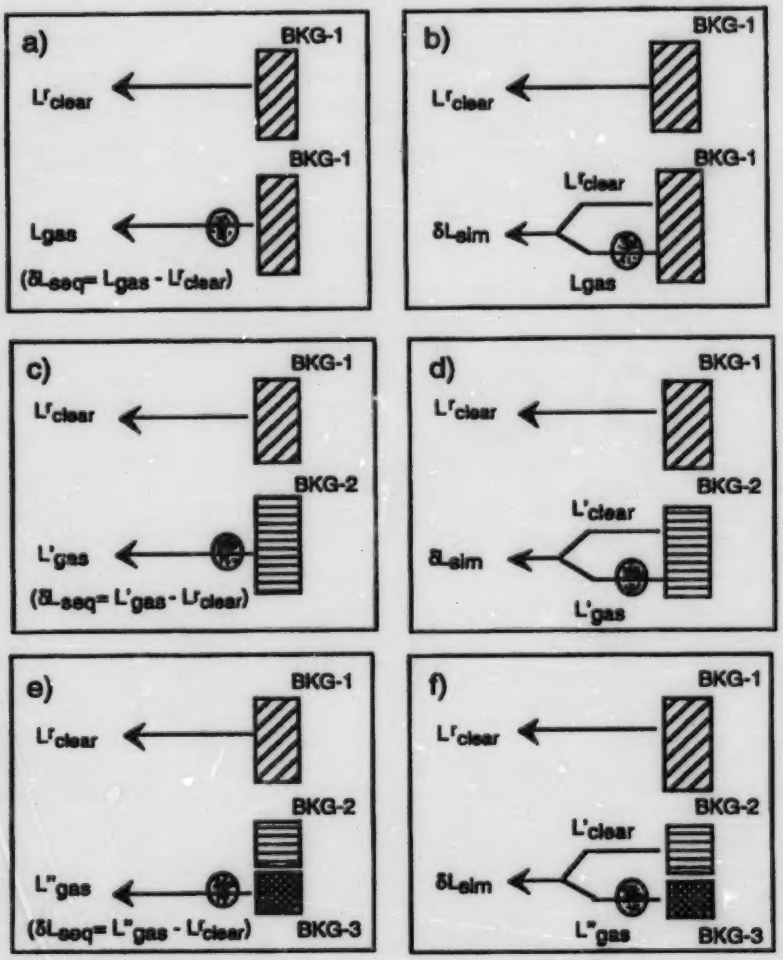

FIGURE 3 - Schematic view of the six scenarios encountered for both sequential and simultaneous background subtraction modes: a- Sequential measurements with a constant background (BKG), b- simultaneous measurements with a constant background, c- sequential measurements with a background variation, d- simultaneous measurements with a background variation, e- sequential measurements with a double background variation, f- simultaneous measurements with a double background variation

2.2.3 Simultaneous Acquisition with Background Variation

To evaluate the impact of a background variation (ΔF) in the simultaneous acquisition approach (Fig. 3d) we write

$$L'_{clear} = F_{bkr}\tau_{near}\tau_{atr} + N_{near} \qquad [15a]$$

$$L'_{clear} = \left(F_{bkr} + \Delta F\right)\tau_{near}\tau_{atr} + N_{near} \qquad [15b]$$

$$L'_{gas} = \left(F_{bkr} + \Delta F\right)\tau_{near}\tau_{gas} + B_{gas}\left(1-\tau_{gas}\right)\tau_{near} + N_{near} \qquad [15c]$$

yielding

$$\delta L_{sim} = \left(L'_{gas} - L'_{clear}\right) = \Delta L_{clear}(\tau_{gas} - 1) + \left(1-\tau_{gas}\right)\left[B_{gas}\tau_{near} + N_{near} - L'_{clear}\right] . \qquad [15d]$$

As seen in Eq. 15d, for the simultaneous acquisition the background variation also introduces an additive term in the radiance differential but in this case it is proportional to the clear-scene radiance variation times the absorbance ($1-\tau_{gas}$) of the target gas. This is the self-compensation effect in simultaneous acquisition. This is a significant result which says that in the simultaneous acquisition mode the radiance differential is less sensitive to background variations especially at low vapor concentrations when the transmittance is close to one. From an operational point of view, this is exactly what is needed, i.e. a system able to detect small amount of chemical vapor which does not require frequent updates for L'_{clear}. By comparisons of Eq. 14c with Eq. 15d, and assuming for instance a gas transmittance of 90% (low concentration), it appears that the sequential acquisition is nine times more impacted by background variations than the simultaneous one for the scenarios reported in Figs. 3c and 3d.

2.2.4 Sequential Acquisition: General Case of Background Variations

The most general scenario of background variations is summarized in Figs. 3e and 3f. In this case it is assumed that the clear-scene radiance can change from L'_{clear} (reference scene) to L'_{clear} (current scene) due to a background variation ΔF_a. An additional variation must also be introduced to take into account the background variation ΔF_b between the current clear scene L'_{clear} and the actual background scene behind the gas L''_{clear} (not identified in

Fig. 3). The superscript ('') associated with L''_{gas} is introduced to express the modification caused by the two background variations, ΔF_a plus ΔF_b. Note that the background variations, ΔF_a and ΔF_b can be caused by a variety of phenomena such as variations induced by the sun heating (temporal), by the sky variability (temporal) and by the background texture variations (spatial). For the sequential acquisition approach we have

$$L'_{clear} = F_{bar}\tau_{near}\tau_{air} + N_{near} \qquad [16a]$$

$$L''_{gas} = \left(F_{bar} + \Delta F_a + \Delta F_b\right)\tau_{near}\tau_{gas} + B_{gas}\left(1-\tau_{gas}\right)\tau_{near} + N_{near} \qquad [16b]$$

yielding

$$\delta L_{seq} = \left(L''_{gas} - L'_{clear}\right) = \left(\Delta L^a_{clear} + \Delta L^b_{clear}\right)\tau_{gas} + \left(1-\tau_{gas}\right)\left[B_{gas}\tau_{near} + N_{near} - L'_{clear}\right] , \qquad [16c]$$

where $\Delta L^a_{clear} = \Delta F_a\tau_{near}$ and $\Delta L^b_{clear} = \Delta F_b\tau_{near}$. As expected, the background variations introduce two additive terms in the radiance differential (Eq. 16c) which are proportional to their respective clear-scene drifts times the transmittance of the target gas. Again because of the high gas transmittance values at low concentrations, a frequent updating of L'_{clear} would be required to minimize the impact of the background drifts on the radiance differential.

2.2.5 Simultaneous Acquisition: General Case of Background Variations

For the general case of background variations (ΔF_a and ΔF_b) in the simultaneous acquisition approach (Fig. 3f) we have

$$L'_{clear} = F_{bar}\tau_{near}\tau_{air} + N_{near} \qquad [17a]$$

$$L'_{clear} = \left(F_{bar} + \Delta F_a\right)\tau_{near}\tau_{air} + N_{near} \qquad [17b]$$

$$L''_{gas} = \left(F_{bar} + \Delta F_a + \Delta F_b\right)\tau_{near}\tau_{gas} + B_{gas}\left(1-\tau_{gas}\right)\tau_{near} + N_{near} \qquad [17c]$$

yielding

$$\delta L_{sim} = \left(L''_{gas} - L'_{clear}\right) = \left[\Delta L^{a}_{clear}(\tau_{gas} - 1) + \Delta L^{b}_{clear}\tau_{gas}\right] + \left(1 - \tau_{gas}\right)\left[B_{gas}\tau_{near} + N_{near} - L'_{clear}\right] . \quad [17d]$$

where again $\Delta L^{a}_{clear} = \Delta F_a \tau_{near}$ and $\Delta L^{b}_{clear} = \Delta F_b \tau_{near}$. As seen in Eq. 17d for the simultaneous acquisition, the two background variations introduce two additive terms in the radiance differential; one being proportional to the gas transmittance and the other one being proportional to the absorbance.

From comparison of the general results obtained at Eqs 16d (sequential) and 17d (simultaneous) it can be concluded that, at low concentration, the radiance differential obtained from simultaneous acquisition is likely less impacted by background variations than the one obtained from sequential acquisition. A consequence of this is that the simultaneous acquisition approach requires less updating for L'_{clear} which facilitates the detection in the operational context of a moving platform or a moving background. This scenario of simultaneous acquisition with background variations corresponds to the general case of acquisition done with the double-beam CATSI instrument. Consequently, the general expression for the calculated radiance differential in simultaneous acquisition is defined by

$$\delta L_{calc} = \left[\Delta L^{a}_{clear}(\tau_{gas} - 1) + \Delta L^{b}_{clear}\tau_{gas}\right] + \left(1 - \tau_{gas}\right)\left[B_{gas}\tau_{near} + N_{near} - L'_{clear}\right] . \quad [17e]$$

Finally, it can be easily verified that if the vapor cloud occupies a fraction f of the field-of-view then the radiance differential would be given by

$$\delta L_{calc} = f\left\{\left[\Delta L^{a}_{clear}(\tau_{gas} - 1) + \Delta L^{b}_{clear}\tau_{gas}\right] + \left(1 - \tau_{gas}\right)\left[B_{gas}\tau_{near} + N_{near} - L'_{clear}\right]\right\} . \quad [17f]$$

For the rest of this work, these expressions (Eqs. 17e and 17f) will be referred to as the calculated radiance differential.

3.0 EXPERIMENTAL ASPECTS OF THE DIFFERENTIAL DETECTION

In the previous chapter the equations for differential detection have been established to compute the theoretical radiance in terms of the gas and background parameters. It is important to recall that in our differential approach two measured spectra are required to process the detection equation; the differential radiance spectrum (δL_{meas}) and the clear-

scene radiance spectrum (L^r_{clear}). An important effort has been spent to develop an instrument and a calibration procedure adapted for both the differential (δL_{meas}) and the direct measurements (L^r_{clear}). In particular, the attributes of our differential approach favor first, the reduction of the temporal background inconsistency by performing an instantaneous optical background subtraction (simultaneous acquisitions, see Chap. 2) and second, the simplification of the radiometric calibration by using a properly balanced double-beam FTIR interferometer. The following sections review the CATSI instrument, the experimental methodology and the procedure of radiometric calibration. Complementary information on this can also be found in Refs. 4 and 5.

3.1 Description of the CATSI instrument

A useful attribute of the Compact Atmospheric Sounding Interferometer (CATSI) system is its optimization for suppressing the background and the instrument self-emission by optical subtraction. As seen on the optical diagram of CATSI (Fig. 4), the reflected beams from corner reflectors are offsetted laterally from the incident beams. This makes it possible to decouple input and output channels, as opposed to the standard single-beam interferometer, and to adjust independently the self-emission from each input port without affecting in any way the output optics, which is not possible with the single-beam configuration. Then the strategy consisted in designing the double-beam interferometer so that the two self-emission terms and the two source terms from each input port can be made equal in intensity and 180° out of phase, leading to a theoretically perfect cancellation.

Essentially, the CATSI instrument is made of two identical 4-in. diameter Newtonian telescopes optically coupled with the dual-beam interferometer. Figure 4 summarizes the optical design and shows the instrument mounted on a tripod. An important effort was dedicated to respect symmetry criteria. The CATSI system allows measurements of spectra according to the following specifications: scene fields of view from 4 to 11 mrad, spectral coverage from 3 to 18 μm, and a spectral resolution of 1 cm^{-1} or greater. A flat plate mirror placed in front of each telescope can be rotated to the selected scene. The pointing capability of this scene mirror allows azimuth measurements from 0 to 180 degrees. Coarse adjustments in azimuth and elevation are simply achieved by rotating the whole assembly mounted on a tripod. After reflection on the scene mirror the input beam is focused by the Newtonian telescope at the entrance of the interferometer and then reflected by an off-axis parabolic mirror to produce a collimated beam of proper diameter in front of the beamsplitter.

A double pendulum scanning mechanism controls the periodic displacement of the two corner reflectors (CC) that generate the interferogram. The beamsplitter consists of a thin air gap ($\lambda/4$ at 7 μm) squeezed between two ZnSe substrates having antireflection coatings on their external faces. Of the two output channels only one is used at this moment. This output module contains parabolic and condensing mirrors that focus the beam onto a sandwich MCT-InSb detector (1 mm) mounted on a microcooler (EG&G Judson): The MCT element is optimized for the 6-18 μm spectral region, while the InSb element is optimized for the 2-5 μm region. Two CCD cameras mounted on the top of the two telescope modules are used to aim at and view the scenes under consideration. With this instrument, two radiance scenes coming from adjacent FOVs are optically combined at the detector level yielding the spectral difference of the scenes. The overall system weighs approximately 18 kg with a linear size of 33 cm.

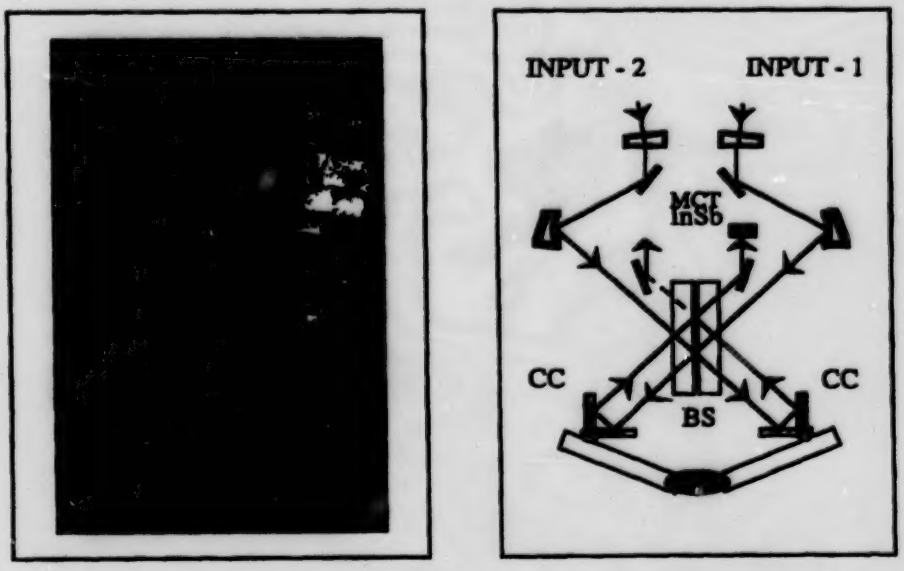

FIGURE 4 - Picture (a) and optical diagram (b) of the Compact Atmospheric Sounding Interferometer (CATSI)

3.2. Equations for the Radiometric Calibration

The following equations serve to establish the radiometric characteristics of the CATSI instrument and to introduce the calibration procedure. For an FTIR spectrometer based on a double input port interferometer the total signal S represents the sum of two individual complex raw spectra, E_1 and E_2, associated with each input ports. If input-1 and input-2 point at the clear-scene radiance (L_{clear}) and the gas-scene radiance (L_{gas}), respectively, the resulting raw spectrum is given by

$$S = E_1 + E_2 \ , \qquad [18]$$

with

$$E_1 = K_1\left(L_{clear} + SE_{in1}\right) \ , \qquad [19]$$
$$E_2 = K_2\left(L_{gas} + SE_{in2}\right) \ , \qquad [20]$$

where, K_1 and K_2 are defined as the responsivities associated with input-1 and input-2, respectively. The terms SE_{in1} and SE_{in2} are the two self-emissions associated with input-1 and input-2, respectively. Each of these terms includes the self-emission from the various optical components of the corresponding input. The self-emission from each ZnSe plate composing the beamsplitter assembly is also included in these terms.

To establish the radiometric calibration of the dual-beam interferometer it is advantageous to proceed by analogy with the single-beam calibration approach. In the particular case where calibration is performed on input-2, while the source on input-1 L_{clear} remains constant and fixed for the three measurements (target and two references) then the corresponding raw spectrum can be written as (using Eqs. 18-20)

$$S = K_2\left(L_{gas} + O_2\right) \ , \qquad [21]$$

with

$$O_2 = \left(SE_{in2} + \frac{K_1}{K_2}L_{clear} + \frac{K_1}{K_2}SE_{in1}\right) \ . \qquad [22]$$

Note that the source L_{clear} which is probed through input-1 can be seen as a part of the instrument offset (O_2). Equations 21 and 22 link the complex raw spectrum S to the radiance spectrum L_{gas} taking into account the characteristics of the double-beam interferometer which are the complex spectral responsivity K_2 and the complex spectral offset O_2 associated with channel-2. The method used to measure these two calibration parameters is the one proposed by Revercomb et al (Ref. 6). It is often referred to as the two-temperature calibration method. In this method, two reference blackbodies of known radiances B_{hot} (hot temperature blackbody) and B_{amb} (ambient temperature blackbody) are used for the measurement of two raw spectra, S_{hot} and S_{amb}. These two raw spectra and radiances defines two calibration equations $S_{hot} = K_2(B_{hot} + O_2)$ and $S_{amb} = K_2(L_{amb} + O_2)$ that are solved to obtain the two unknowns, yielding

$$K_2 = \frac{S_{hot} - S_{amb}}{B_{hot} - B_{amb}}, \qquad [23]$$

and

$$O_2 = \frac{S_{amb}B_{hot} - S_{hot}B_{amb}}{S_{hot} - S_{amb}}. \qquad [24]$$

When applied to an optically balanced double-beam interferometer this radiometric calibration can be simplified. From Eq. 22 it can be seen that the spectral offset O_2 associated with channel-2 can be minimized by the fulfillment of two system conditions: First, the condition of balanced responsivities ($K_1 = -K_2 = K_2 e^{i\pi}$) and second, the condition of balanced emissions ($SE_{in1} = SE_{in2}$). When these two conditions apply, the resulting raw spectrum (Eqs. 21-22) reduces to

$$S = K_2(L_{gas} - L_{clear}). \qquad [25]$$

In this form, Eq. 25 does not contain a self-emission term from the instrument. The resulting raw spectrum S is directly proportional to the spectral difference between the two source radiances and consequently, the measured radiance differential is given by

$$\delta L_{meas} \equiv \left(L_{gas} - L_{clear}\right) = \frac{S}{K_2} \quad . \qquad [26]$$

The use of an optically balanced double beam FTIR interferometer considerably simplifies the radiometric calibration where in principle only one reference measurement is needed to evaluate the spectral responsivity K_2 of the instrument (no offset).

The above equations (Eqs. 25-26) summarize the strategy pursued in the development of the CATSI instrument, i.e. an optically balanced interferometer with no self-emission terms. However, in practice we have found that with the current CATSI system there are some limitations. For example, Fig. 5 shows the measured radiance of a blackbody at 15°C (upper curve) and the resulting difference when the two input ports view the same blackbody (15°C). The suppression effect is obvious. However the resulting difference (bottom curve) is not exactly zero. Above 700 cm^{-1} the residual is of the order of a few percents and in the 500 to 700 cm^{-1} region the spectral residual is of the order of 15%. After investigation we came to the conclusion that these residuals arise from the limited performance of the beamsplitter. An undesired dissymmetry between the optical properties of the two ZnSe substrates forming the beamsplitter was found. This is partly due to non-identical antireflection coatings present on the external face of each substrate, and partly due to a difference between the transmission associated with each substrate. Both effects introduce a dissymmetry such that $SE_{in1} \neq SE_{in2}$ and $K_1 \neq -K_2$.

Because of this anomaly and to achieve the level of accuracy required for the standoff detection of chemicals, the instrument residual emission re_2 has to be taken into account. In this context, Eq. 25 is modified to include the instrument residual, yielding

$$S = K_2\left[\left(L_{gas} - L_{clear}\right) + re_2\right] \quad , \qquad [27]$$

where re_2 is obtained by regrouping the terms in Eqs. 21 and 22 in a more convenient form, i.e.

$$re_2 = \left(1 + \frac{K_1}{K_2}\right)L_{clear} + \left(SE_{in2} + \frac{K_1}{K_2}SE_{in1}\right) \quad . \qquad [28]$$

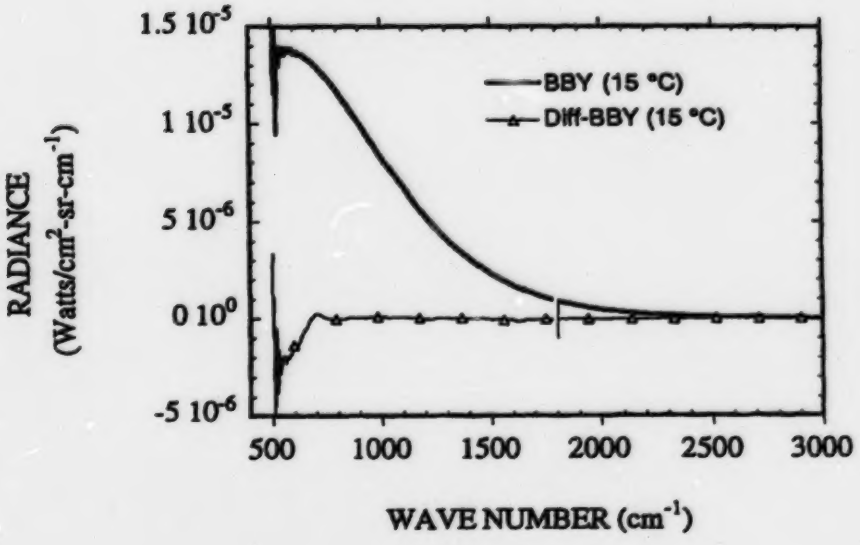

FIGURE 5 - Calibrated measurement of a blackbody at 15°C (upper curve) and the resulting difference when the two ports are used

In a recent paper (Ref. 5), it has been shown that if the two self-emission terms SE_{in1} and SE_{in2} arise essentially from the beamsplitter, emissions from other components being balanced, then the intrument residual can be modeled by

$$re_2 = \left(1 + \frac{K_1}{K_2}\right)\left[L_{clear} - B_s\right], \qquad [29]$$

where B_s is the known Planck radiance related to the beamsplitter temperature. Note that in the CATSI interferometer, the beamsplitter temperature is continuously probed by an internal sensor fixed on the beamsplitter holder. Equation 29 is a simple and useful relation which gives the instrument residual of the double-beam interferometer with an optical dissymmetry between the two beamsplitter substrates. This dissymmetry has the consequence that in certain spectral regions the responsivities K_1 and K_2 are not fully balanced.

3.3 Procedure for the Radiometric Calibration

As discussed above, in our differential approach two measured spectra are required as inputs to the detection equation, i.e. the differential radiance spectrum (δL_{meas}) and the clear-scene radiance spectrum (L'_{clear}). In the following we present the calibration procedure that allow the measurement of these two spectra. It is complicated by the fact that we have to evaluate the instrument residual emission re_2 which cannot be eliminated because of the beamsplitter anomaly.

After a period of investigation to find an optimum way to operate the current CATSI intrument for standoff detection experiments we have retained a two-step procedure. The first step consists in evaluating the two calibration parameters and the clear-scene radiance. It consists of a series of three consecutive acquisitions where the telescope associated with input-2 is successively aimed at a hot reference blackbody (60°C), at an ambiant reference blackbody (~ 25°) and at the clear-scene (L'_{clear}). It is important to note that, in the current procedure, the telescope associated with input-1 (reference telescope) is aimed at the same clear-scene (L'_{clear}) for each of the three measurements. In this context the three equations for the measured spectra associated with each acquisitions are

$$S_{hot} = K_2\left[\left(L_{hot} - L'_{clear}\right) + re_2\right] , \qquad [30]$$

$$S_{amb} = K_2\left[\left(L_{amb} - L'_{clear}\right) + re_2\right] , \qquad [31]$$

$$S_{clear} = K_2\left[re_2\right] . \qquad [32]$$

L_{hot} and L_{amb} represent the radiance associated with the hot and the ambiant blackbodies, respectively. The two calibration parameters of the instrument (K_2) and (re_2), and the clear-scene radiance term L'_{clear} can all be obtained from Eqs. 30-32 where

$$K_2 = \left(\frac{S_{hot} - S_{amb}}{L_{hot} - L_{amb}}\right) , \qquad [33]$$

$$re_2 = \frac{S_{clear}}{K_2} \quad , \qquad [34]$$

and

$$L'_{clear} = L_{hot} - \frac{S_{hot}}{K_2} + re_2 \quad . \qquad [35]$$

It is recalled that the known quantities are the calculated blackbody radiances L_{hot} and L_{amb}, and the three measured raw spectra S_{hot}, S_{amb}, and S_{clear}. As discussed in Chapter 2, the measured L'_{clear} spectrum given by Eq. 35 is one of the two measured spectra used in Eqs. 17d (right-hand side) for achieving the detection. The current calibration sequence takes approximately three minutes of acquisition (one minute for each source) to obtain the required accuracy for the calibration parameters (K_2,re_2) and L'_{clear} at a spectral resolution of 4 cm^{-1}.

The second step of the measurement procedure consists in generating the current spectral radiance differential (δL_{meas}). In this case the telescope associated with input-2 is aimed at the target-gas-scene (L_{gas}) while the telescope associated with input-1 remains pointed in the direction of a consistent clear scene (L_{clear}). Note that the clear-scene radiance, L_{clear}, intervening in step-2 may be different from the reference measurement, L'_{clear}, recorded at step-1. Each differential raw spectrum (S) generated this way is then automatically calibrated by application of Eq. 27 yielding the calibrated radiance differential

$$\delta L_{meas} = \frac{S}{K_2} - re_2, \qquad [36]$$

where the two calibration parameters, K_2 and re_2, have been previously obtained at step one (Eqs. 33 and 34). The main source of errors in the resulting δL_{meas} comes from the calibration parameters (K_2, re_2). Ideally these parameters would be updated as often as possible. The responsivity K_2 is mainly affected by the slow thermal drift of the instrument. The instrument residual re_2 (Eq. 29) mainly depends on the clear-scene radiance changes between step-1 and step-2 (from L'_{clear} to L_{clear}). In practice we have found it satisfactory to update the calibration parameters every half hour. Over this period of time, the responsivity

K_2 is always stable but the instrument residual re_2 may change significantly. In this case, Eq. 36 should be slightly modified to take into account a possible drift Δre_2 due to a clear-scene radiance change ΔL^s_{clear} yielding for the radiance differential

$$\delta L_{meas} = \frac{S}{K_2} - (re_2 + \Delta re_2), \qquad [37]$$

with

$$\Delta re_2 = \left(1 + \frac{K_1}{K_2}\right)\Delta L^s_{clear}, \qquad [38]$$

where a perturbation form of Eq. 29 has been used to generate Eq. 38. It is important to note that the radiance change ΔL^s_{clear} is identical to the clear-scene radiance drift between the reference measurement (L^r_{clear}) and the actual measurement (L^r_{clear}) such as discussed in Sec. 2.2.5 and illustrated in Figs. 3d and 3f.

Because the responsivity ratio K_1 / K_2 is not directly evaluated through the calibration process it is convenient to rewrite Eq. 38 in terms of known quantities by using the identity of Eq. 29 yielding

$$\Delta re_2 = \left(\frac{re_2}{L^r_{clear} - B_s}\right)\Delta L^s_{clear}, \qquad [39]$$

where again B_s is the known Planck radiance associated with the beamsplitter temperature, and re_2 and L^r_{clear} are evaluated through the calibration process (step-1). Finally the general expression for the measured radiance differential which takes into account a first order drift in the clear-scene radiance is given by

$$\delta L_{meas} = \frac{S}{K_2} - re_2 - \left(\frac{re_2}{L^r_{clear} - B_s}\right)\Delta L^s_{clear}, \qquad [40]$$

where it is emphasized that the only unknown quantity is the clear scene radiance drift ΔL^s_{clear}.

As an example of the measurement procedure with the CATSI instrument, Fig 6 summarizes a typical result of standoff detection for a chemical vapor of SF_6 located at a distance of 460 m. The SF_6 vapor, at ambiant temperature (28° C), is observed horizontally againts a background scene approximately 1.4° C warmer. Figures 6a and 6b represent the calibration parameters, K_2 and re_2, derived from the calibration procedure (step-1) and computed by Eqs. 33 and 34. As seen, the responsivity (Fig. 6a) exibits a fairly constant modulus and a linear phase variation in the 800 to 1200 cm^{-1} spectral region which is a standard trend for an FTIR spectrometer operated with an MCT detector. Because of the imperfect suppression with the current CATSI beamsplitter, the modulus of the instrument residual (Fig. 6b) is not exactly zero. It peaks at a value of approximately 4% of the clear-scene radiance and the phase is fairly close to zero in the 800 to 1200 cm^{-1} spectral region. Figure 6c shows the resulting clear-scene radiance (L^r_{clear}) obtained at step-1 and calculated by Eq. 35. The clear-scene is mainly composed of conifers and exibits a blackbody type radiance. Finally, the radiance differential (δL_{meas}) evaluated at step-2 is shown in Fig. 6c where in this example the clear-scene radiance drift (Δre_2) was arbitrarily neglected, i.e $\Delta L^a_{clear} = 0$ in the computation with Eq. 40. As expected, δL_{meas} exibits a fairly flat trend in the 800 to 1200 cm^{-1} region from which the SF_6 signature is easily identified even though it represents only about 1% of the background signal (L^r_{clear}). This illustrates well the difficulties encountered in detection with background-to-signal ratio of the order of 100. It is believe that our differential approach is particularly appropriate for this purpose. The small positive offset ($6x10^{-8}$ $Watts/cm^2\text{-}sr\text{-}cm^{-1}$) observed throughout the band is probably due to a slight difference between the background behind the vapor compared with the adjacent background scene.

In summary, the calibration procedure used to generate the radiance differential δL_{meas} is not instantaneous in the sense that it uses parameters (K_2, re_2, L^r_{clear}) usually recorded in the previous half hour. Over this period of time, the responsivity (K_2) of the instrument is generally quite stable but the instrument residual (re_2), through the clear-scene term, can change enough to create problems in the vapor detection process. For this reason, it appeared convenient to introduce a first order correction that takes into account the clear-scene radiance drift ΔL^a_{clear}. Although this parameter is not know it will be shown, in the next chapter, how the detection algorithm can handle this clear-scene drift by using a proper fitting process.

P515096.PDF [Page: 32 of 86]

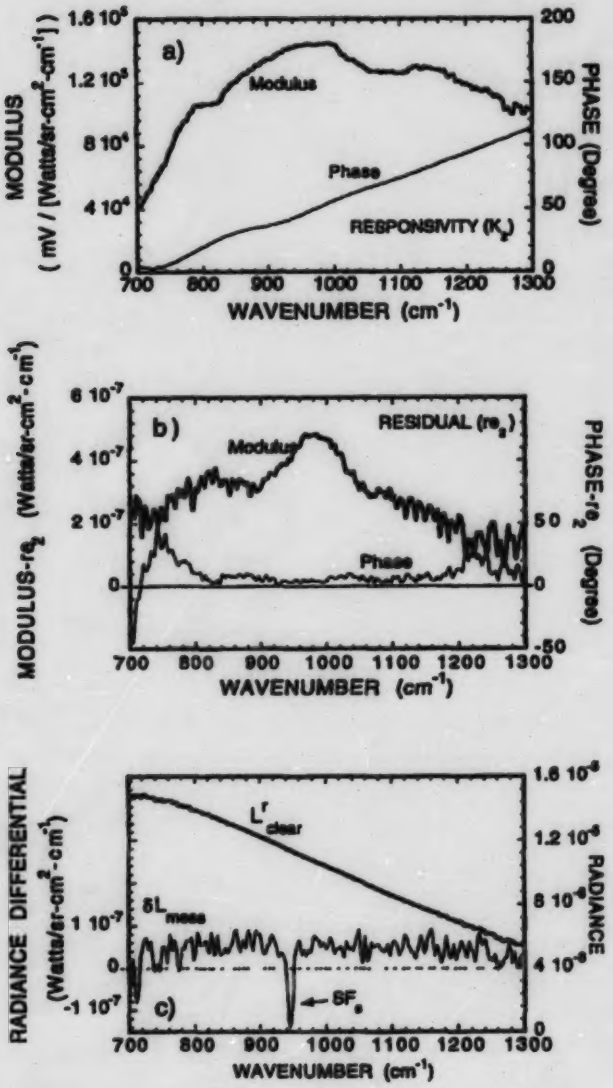

FIGURE 6 - Typical calibration and measurement with CATSI: (a)- The instrument responsivity, K_2, (b)- the instrument residual, re_2, and (c)- the measured clear-scene radiance, L^r_{clear}, and the measured differential for a vapor of SF_6 at a distance of 460 m

3.4 Advantages of the Double-beam Interferometer for Differential Detection

Figure 6c summarizes well the level of accuracy and the issues encountered in the standoff detection of chemical vapor that usually implies low signal levels and very high background signals. In this case, even small errors in the background radiance evaluation may appear large compared with the vapor signal itself. Differential detection is seen as one, if not the best approach to handle certain experimental constraints associated with these conditions of low target-to-background ratio. Differential detection may be achieve in several different ways. It can be done with a single beam FTIR interferometer by combining two consecutive measurements, i.e. background with / without cloud vapor. The single beam instrument can also be used with a detector array to achieve the differential detection from detector pixels subtraction. Finally, a double-beam interferometer such as CATSI can be used to perform differential detection by optical subtraction. From a theoretical standpoint, these three approaches are somewhat equivalent. From an experimental point of view, the configuration of the instrument (single or double beam) and the protocol used to obtain the calibrated radiance differential are critical in determining the error associated with the measurements. This aspect is addressed below.

To simplify the demonstration, let us assume that the FTIR instrument used is a perfectly balanced double-beam interferometer. In this case, the instrument residual is equal to zero ($re_2 = 0$). This instrument can be used either in the single-beam configuration or in the double-beam configuration (this simplifies the comparison). In the single-beam configuration a known reference (L_{ref}) such as a flat plate blackbody is attached to input-1. In this case, the gas-scene radiance (L_{gas}) is connected to the raw spectrum (S) and the responsivity (K_2) by

$$L_{gas} = \frac{S_{gas}}{K_2} + L_{ref}, \qquad [41]$$

where Eq. 26 has been adapted for the single-beam configuration by replacing the clear-scene radiance with L_{ref}. Similarly, the clear-scene radiance is given by

$$L_{clear} = \frac{S_{clear}}{K'_2} + L_{ref}, \qquad [42]$$

where K'_2 represents the responsivity for the clear-scene measurement which can be different if, for instance, a different detector pixel is used for subtraction. Assuming an error on each responsivity (ΔK and $\Delta K'$), then the resulting radiance errors are given by

$$\Delta L_{gas} = -\frac{S_{gas}}{K_2^2}(\Delta K) \qquad [43a]$$

or

$$\Delta L_{gas} = -\left(L_{gas} - L_{ref}\right)\left(\frac{\Delta K}{K_2}\right). \qquad [43b]$$

and

$$\Delta L_{clear} = -\frac{S_{clear}}{K'^2_2}(\Delta K'), \qquad [44a]$$

or

$$\Delta L_{clear} = -\left(L_{clear} - L_{ref}\right)\left(\frac{\Delta K'}{K'_2}\right). \qquad [44b]$$

Moreover, if the two responsivity errors, ΔK and $\Delta K'$, are uncorrelated then the error on the radiance differential can be estimated by

$$\left|\Delta(\delta L)\right| = \left|\left(L_{gas} - L_{ref}\right)\left(\frac{\Delta K}{K_2}\right)\right| + \left|\left(L_{clear} - L_{ref}\right)\left(\frac{\Delta K'}{K_2}\right)\right|, \qquad [45]$$

where the absolute values are combined to take into account the uncorrelated nature of the responsivity errors. In this context, the radiance differential error, $\left|\Delta(\delta L)\right|$, represents the amplitude rather than the variance of the error trend. Equation 45 is an important result that helps assess the accuracy of various detection methods. For instance, in the single-beam approach a large error in the radiance differential can happen if the radiance of the reference (L_{ref}) is low. For instance, in direct detection (as opposed to differential) a common practice consists in using a cold reference such as liquid nitrogene ($L_{ref} \sim 0$). In this case, Eq. 45 can be approximated by

$$|\Delta(\delta L)| \approx 2L_{clear}\left(\frac{|\Delta K|}{K_2}\right), \qquad [46]$$

where the two assumptions, $L_{gas} \sim L_{clear}$ and $|\Delta K| \sim |\Delta K'|$, have been used. Because the radiance differential is usually of the order of 1% of the L_{clear} radiance, and assuming 0.5% as a typical error on the responsivity, then Eq. 46 yields a 100% error on the radiance differential. Thus, the single-beam configuration with cold reference should be avoided for differential detection. The best configuration can be deduced by inspection of Eq. 45. The minimum error on the radiance differential is obtained when the reference, L_{ref} is equal to the clear-scene radiance (L_{clear}). This corresponds to the case of differential detection by simultaneous acquisition with a double-beam instrument such as CATSI. In this case, Eq. 45 reduces to

$$|\Delta(\delta L)| = (L_{gas} - L_{clear})\left(\frac{|\Delta K|}{K_2}\right) = \delta L\left(\frac{|\Delta K|}{K_2}\right), \qquad [47]$$

where now a 0.5% error on the responsivity yields a 0.5% on the radiance differential which is two order of magnitude more accurate than the single-beam approach with a cold reference.

Equation 45 expresses the fact that the radiance of the reference source has a critical impact on the detection accuracy. Because of the optical subtraction mechanism intervening in the interferometer, when the radiance of the reference source (L_{ref}) is large, the magnitude of the resulting raw spectrum (S) is small. Conversely, when the radiance of the reference source is small ($L_{ref} \sim 0$), the magnitude of the resulting raw spectrum (S) is large. As indicated by Eqs. 43a, the absolute error on the radiance is proportional to the magnitude of the raw spectrum, which means that large absolute errors on L_{gas} and L_{clear} happen when the reference source is small ($L_{ref} \sim 0$). The difference of these two large values yields a radiance differential with a large absolute error. For this reason, it is advantageous to minimize the magnitude of the raw spectrum (S) by chosing a reference source that matches as much as possible the clear scene radiance ($L_{ref} \sim L_{clear}$). In this respect, our approach with the double-beam interferometer, i.e. input-2 on L_{gas} and input-1 on L_{clear}, appears particularly convenient because the gas-scene and clear-scene subtraction is directly done at

the optical level, because the reference scene is automatically of the right magnitude, and because there is no need for a reference source.

For the sake of completeness, it should be noted that, in the case of systematic errors, identical on both responsivities ($\Delta K = \Delta K'$), it can be shown that the resulting error on the radiance differential is independent of L_{ref} and is given by eq. 47 which represents the optimum solution.

4.0 MODELING AND ALGORITHM DEVELOPMENTS

There exist many processing methods developed for the passive standoff detection of chemical vapors. Kroutil and collaborators (Ref. 1) have described several of them. Some new or updated methods have also been proposed recently, such as the orthogonal digital filtering method for background removals (Ref. 2), the principal component analysis approach (Ref. 3), the linear discriminant analysis for pattern recognition in the interferogram domain and in the frequency domain (Refs. 7-11), and the special ratio algorithm for quantitative analysis (Ref. 12). Each of these methods have strengths and weaknesses, depending on the scenario under consideration, i.e. up-looking or down-looking scenarios.

The differential FTIR detection method we propose in the present work has a unique attribute with regard to background removal, i.e., the method efficiency is approximately insensitive to the background type. With this method, the two probed scenes (gas and clear scenes) are optically combined onto a single detector, resulting in a real-time optical subtraction. This yields a cloud vapor spectrum minimally perturbed by the background radiation. To explore and exploit the attributes of this differential detection method we have developed a processing algorithm referred to as the GASEM (Gaseous Emission Monitoring) algorithm. GASEM is not an advanced algorithm for automatic detection and identification. Rather, it represents a step-gap prototype that will lead to constructing an advanced version for automatic detection.

In several detection approaches, the algorithm development is driven by the search for a universal and very robust processing algorithm able to extract the target-vapor spectral information with a minimum of a-priori knowledge regarding the radiometric calibration of the instrument, the spectral contributions from the atmospheric interferents and the spectral

features of the background environment. We have been pursuing a different but complementary approach for GASEM. In our case, a special effort has been dedicated to better control this a-priori knowledge for the benefit of the detection process. For instance, the radiometric calibration has been simplified by using an optically balanced interferometer (CATSI), the background scene component is optically subtracted in real-time at the instrument level (CATSI), and the GASEM algorithm includes a built-in model to take into account the spectral contributions from atmospheric interferents and from the background environment.

In its current form, GASEM is built to support three basic tasks. First, it controls the interferometer acquisition, second it performs the fitting computations to retrieve on-line the selected gas, atmosphere and background parameters, and third it displays the parameters as a function of time. The instrument continuously co-adds the incoming spectra and periodically sends the current mean to the processing program. The overall process of acquisition, processing and display is performed on-line. More technical information concerning the algorithm approach and the software options can be found in Refs. 13 and 14. In the following section, the main modeling and processing components of GASEM are described together with several examples to emphasize the attributes of the actual algorithm.

4.1 Minimization by SIMPLEX

To illustrate the spectral matching operation involved in the parameters retrieval process that leads to chemical detection and identification, Fig 7a shows a typical standoff measurement (104 m) of the spectral radiance differential for a vapor of methanol (305 ppm-m) in the 800-1200 cm^{-1} (8-12μm) region. In Fig 7b, the same measured spectrum is compared with a series of calculated spectra corresponding to different cloud vapor temperatures varying from 288 K to 304 K. Note that, for the calculations, the spectral band is centered and restricted to the useful part of the methanol band from 950 to 1100 cm^{-1}. As seen with this single-parameter fitting scenario, the best spectral match is approximately obtained for a vapor temperature of 300 K. For the highest vapor temperature of 304 K, the calculated emission spectrum is too high, while for the lowest temperature of 288 K the calculated spectrum is too low and exhibits transmission rather than emission features. Actually, the apparent background temperature correspond to the transit point between transmission and emission features, i.e. a temperature between 292 K and 295 K. The above discussion introduces the processing algorithm with a qualitative example based on a single

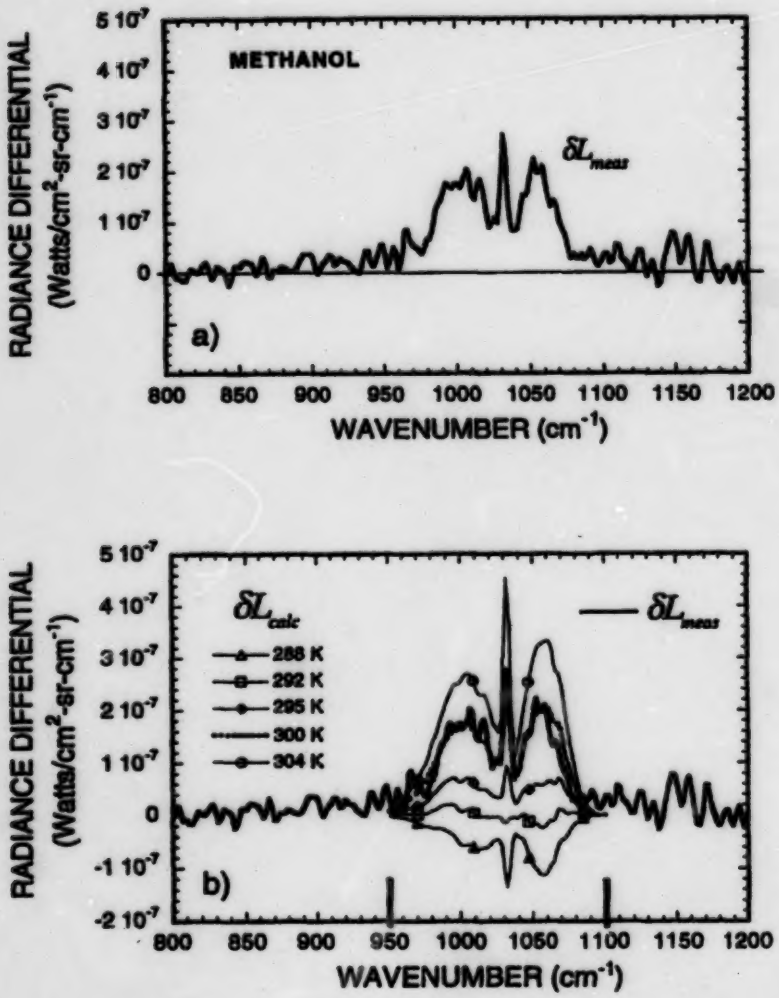

FIGURE 7 - **Illustration of the spectral matching between measured and calculated radiance differentials for the methanol vapor (305 ppm-m) in the 950-1100 cm^{-1} absorption band: a) represents the measured spectrum, and b) are the spectra calculated in the 950-1100 cm^{-1} absorption band of methanol for different vapor temperatures from 288 K to 304 K. A good match is obtained at 300 K.**

parameter retrieval, i.e. the temperature of the chemical cloud. In a similar way but in a more general context, the actual GASEM algorithm has been constructed to perform multi-parameter retrievals to take into account not only the chemical gas parameters (CL and temperature) but also auxiliary parameters characterizing the actual atmospheric and background environment.

It is remembered from Chap.2 (Eq. 17f) that in the simultaneous differential detection mode the calculated spectral radiance differential is given by

$$\delta L_{calc} = \delta L^{\circ}_{calc} + \Delta_{calc} . \qquad [48]$$

where

$$\delta L^{\circ}_{calc} = f\left(1-\tau_{gas}\right)\left[B_{gas}\tau_{near} + N_{near} - L^{r}_{clear}\right] , \qquad [49]$$

$$\Delta_{calc} = f\left[\Delta L^{a}_{clear}(\tau_{gas}-1) + \Delta L^{b}_{clear}\tau_{gas}\right] . \qquad [50]$$

Similarly, the expression for the measured spectral radiance differential as derived in Chap. 3 (Eq. 40) corresponds to

$$\delta L_{meas} = \delta L^{\circ}_{meas} + \Delta_{meas} . \qquad [51]$$

where

$$\delta L^{\circ}_{meas} = \frac{S}{K_2} - re_2 , \qquad [52]$$

$$\Delta_{meas} = -\left(\frac{re_2}{L^{r}_{clear} - B_s}\right)\Delta L^{a}_{clear} . \qquad [53]$$

Here δL°_{calc} (Eq. 49) is interpreted as the calculated radiance differential for the ideal case of no background drifts (i.e. $\Delta L^{a}_{clear} = 0$ and $\Delta L^{b}_{clear} = 0$), and Δ_{calc} (Eq. 50) is seen as an additive correction resulting from the background drifts. Similarly, δL°_{meas} (Eq. 52) is defined as the radiance differential measured with the CATSI instrument for the ideal case of no background drifts (i.e. $\Delta L^{a}_{clear} = 0$), and Δ_{meas} (Eq. 53) is an additive correction to take

into account the background drifts. The calculated (δL_{calc}) and the measured (δL_{meas}) radiance differentials are both sensitive, but in a different way, to the background radiance drifts. Also note that for a perfectly balanced instrument, the instrument residual re_2 vanishes, yielding $\Delta_{meas} = 0$.

The basic processing strategy behind the GASEM algorithm consists in adjusting a set of selected gas, atmospheric and background parameters to produce a calculated spectrum (δL_{calc}) that best fits the spectral features of the measured spectrum (δL_{meas}). In a more quantitative terms and according to the previous equations, the minimization equation can be written as

$$\min \sum_{\nu_{min}}^{\nu_{max}} \left([\delta L^*_{calc} + \Delta_{calc}] - [\delta L^*_{meas} + \Delta_{meas}] \right)^2 . \qquad [54]$$

There exist many different algorithms that can be used to minimize the residual between the measured data and the data calculated according to a set of independent variables (Ref. 15). The one chosen for GASEM is the SIMPLEX algorithm (Ref. 16). A good description of this algorithm can be found in Refs. 15 and 17 and several aspects concerning its implantation have been discussed in Ref. 13. For such an algorithm, initial estimates are required for the selected parameters to be retrieved. After setting the precision and a maximum number of iterations, the SIMPLEX algorithm operates by successive modifications of the selected parameters until a minimum residual (Eq. 54) is reached, yielding the best fitted parameters for this case. The SIMPLEX algorithm has several strong advantages for real-time applications. As discussed in Refs. 13 and 17, the algorithm is remarkably fast, there is no need for numerical differentiation and divergence is almost impossible or at least can be avoided in most of the cases.

4.2 Input and Retrieved Parameters

The calculated radiance differential (δL_{calc}) intervening in the minimization equation is based on a radiative transfer model that uses several gas (chemical vapor), atmospheric and background parameters. Some of these parameters are defined as inputs, known from a-priori considerations, and some others are defined as outputs to be retrieved from the minimization process. In this context, the detection and identification of a given chemical is achieved when the retrieved parameters are physically acceptable and when a high level of

correlation between calculated and measured spectra is obtained. To be clear and because there are several input and output variables involved in the minimization equation, it is convenient to list and discuss each of the intervening terms and their associated parameters (see Eqs. 48 to 54):

f_c;... is the cloud filling factor (Eqs. 49-50). It represents the fraction of the field of view occupied by the cloud. In GASEM, this parameters can be defined either as a known input (usually f=1) or as a retrievable parameter.

τ_{gas};... is the cloud vapor transmittance (Eqs. 49-50). By order of importance this is the leading term because it intervenes in the cloud vapor emissivity (Eq. 49) and also in the clear-scene radiance drifts (Eq. 50). It is modeled by the Beer-Lambert law (see Eq. 3) such that

$$\tau_{gas} = \exp(-\alpha_v CL). \qquad [55a]$$

Note that if there are N chemical species composing the cloud vapor then the corresponding transmittance expression would be given by

$$\tau_{gas} = \exp\left(-\sum_{n=1}^{N}(\alpha_v CL)_n\right). \qquad [55b]$$

The current GASEM algorithm is built to support the retrieval for mixtures composed of up to ten species. Until now the validation and fine tuning of this capability has been limited to only single component and binary mixtures.

α_v;... is the spectral absorption coefficient (1/ppm-m) of the chemical vapor (Eq. 55). This is the central input parameter for the retrieval because it represents the spectral signature of the suspected chemical. As an example, four absorption coefficient spectra are reported in Fig. 8 for vapors of SF_6 (simulant), GB (sarin nerve gas), ammonia and methanol.

CL;... is the cloud vapor integrated-path concentration in unit of ppm-m (Eq. 55). This is one of the major output parameter to be retrieved from the minimization process. Note that, when there are more than one species, GASEM can in principle retrieve each CL species provided that the corresponding α_{nv} is known.

L^r_{clear};... is the clear-scene radiance spectrum recorded prior to the differential measurement (Eq. 49). This is a requested input for the retrieval. It strongly varies with the background scene (sky, ground, trees etc.). An example of a measured clear-scene radiance for a background composed of trees (mainly spruces) at a distance of 500 m is shown in Fig. 9a. The corresponding spectral brightness temperature (T_B) is reported at Fig. 9b. The brightness temperature of a scene is simply defined as the temperature that a blackbody would have to generate the same amount of radiance at a given wavenumber. It is computed using the inverted Plank radiance formula, i.e.,

$$T_B(L_{clear}) = \frac{1.439\nu}{\ln\left(\frac{1.191\times10^{-12}\nu^3}{L^r_{clear}}+1\right)}. \qquad [56]$$

As seen in Fig. 9b, this representation of the clear-scene emission in the form of a brightness temperature facilitates the inter-comparison between different spectral bands. For instance, the ozone spectral feature appearing in the 975 to 1075 cm^{-1} region is well contrasted in the brightness temperature spectrum while it cannot be distinguished in the radiance spectrum. This ozone feature is essentially due to the down-welling IR emission of the atmospheric ozone that is diffusely reflected by the background trees. The complex non-constant behavior of the spectral brightness temperature (Fig. 9b) in the 600 to 1400 cm^{-1} region is partly due to the intervening atmosphere, the background-scene emissivity and the background-scene reflectivity.

B_{gaz};... is the Planck (or blackbody) radiance associated with the cloud vapor (Eq. 49). This term is given by

$$B_{gaz} = \left(\frac{1.191\times10^{-12}\nu^3}{e^{\left(\frac{1.439\nu}{T_{gaz}}\right)}-1}\right). \qquad [57]$$

T_{gaz};... is defined as the temperature of the cloud vapor (Eq. 57). Such as for the CL, this temperature (T_{gaz}) is an important parameter that controls the amount of radiation emitted by the chemical cloud. In GASEM, it can be defined either as a known input or as a retrievable parameter. In any case, T_{gaz} is automatically settled to the clear-scene brightness temperature

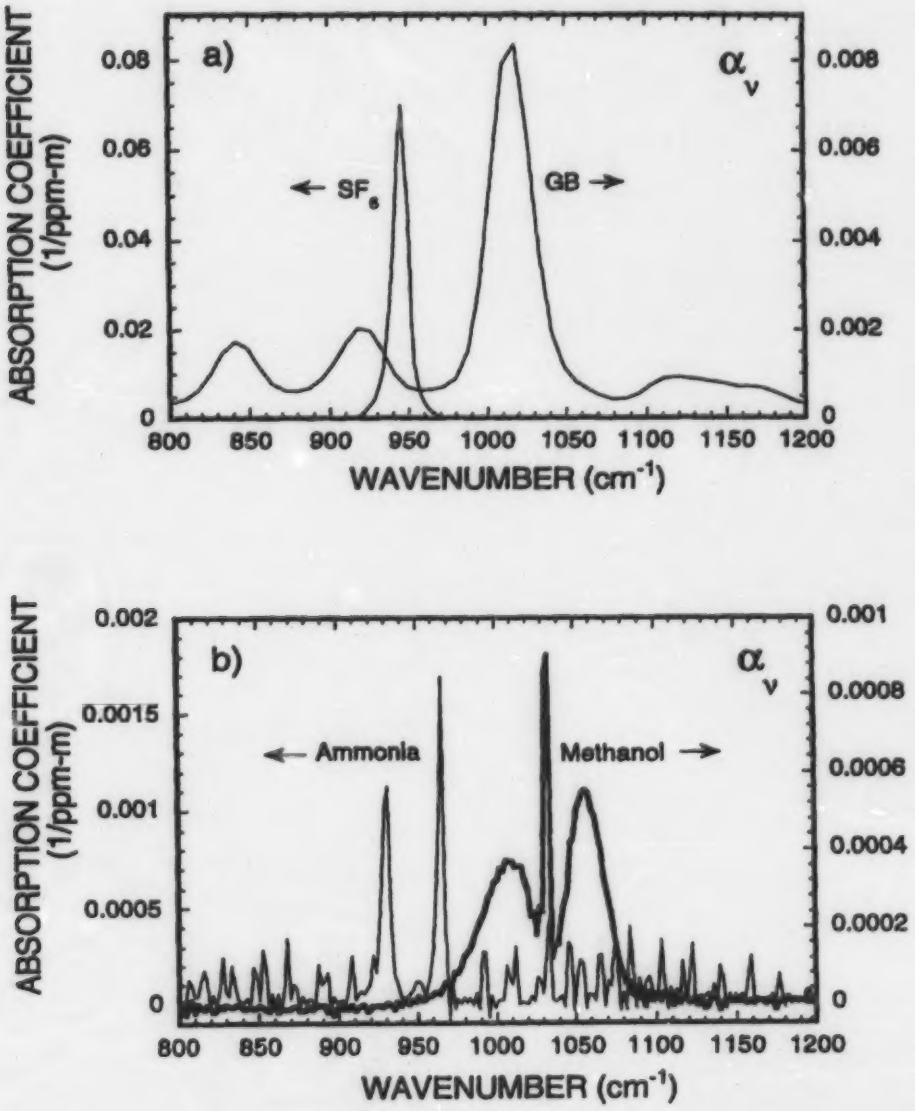

FIGURE 8 - Examples of absorption coefficients for vapors of a simulant, SF_6 (a), of a nerve gas, GB (a), and of two precursors, ammonia and methanol (b).

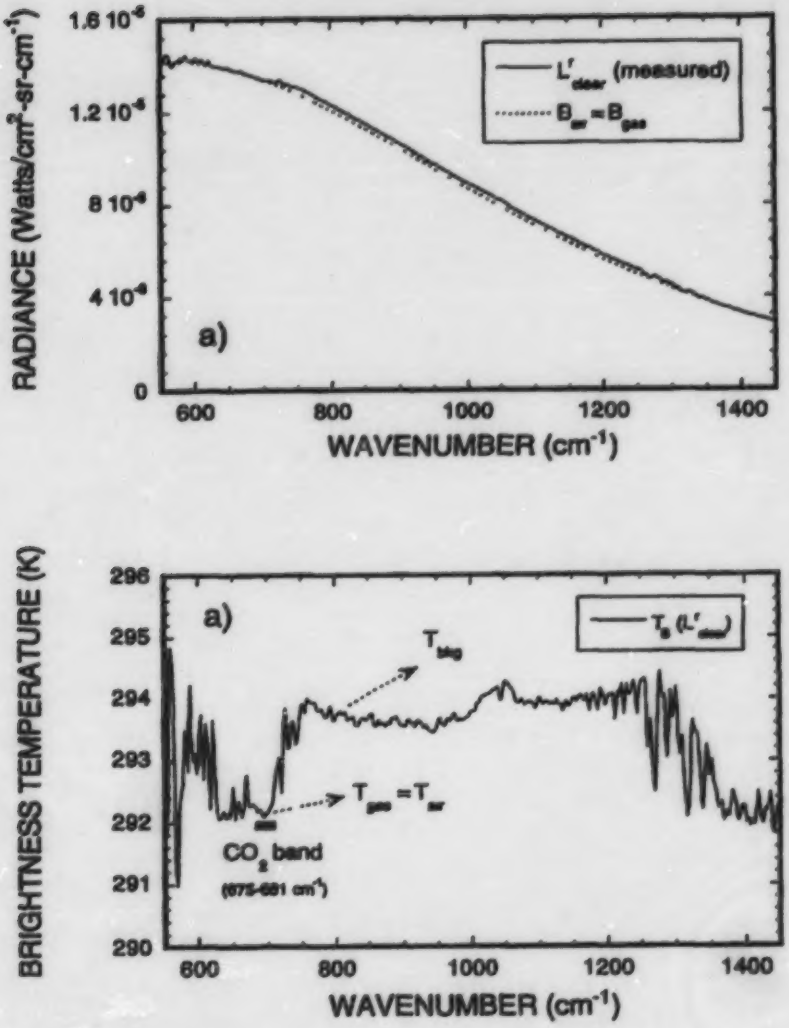

FIGURE 9 - a) Example of a clear-scene radiance spectrum ($L^{\prime}_{clear}$) corresponding to a background composed of trees (at 500 m) compared with the radiance of a blackbody at ambient temperature. b) the spectral brightness temperature associated with the clear-scene radiance ($L^{\prime}_{clear}$).

found in the narrow region from 675 to 681 cm^{-1} (see Fig. 9b). In this spectral region, a strong CO_2 absorption band dominates and the atmosphere is completely opaque. Because of this opacity, the radiation emitted by the atmosphere corresponds to the emission of a blackbody at the ambient-air temperature (T_{air}) near the receiver. For instance, in the example given at Fig. 9b, the ambient-air temperature derived from the CO_2 band corresponds to 292.2 K. When the cloud vapor is in thermal equilibrium with the ambient air i.e., $T_{gas} = T_{air}$, then the clear-scene brightness temperature radiance (675 to 681 cm^{-1}) can be directly used to estimate the gas temperature and to compute the corresponding B_{gas} radiance. An example of B_{gas} radiance computed with the brightness temperature at 292.2 K is also reported in Fig. 9a. In the current GASEM version, the ambient air temperature and the gas temperature are both settled by default to the clear-scene brightness temperature recorded in the 675 to 681 cm^{-1} region. Note that the brightness temperature in the transmission window from 800 to 1200 cm^{-1}, is representative of the background-scene. Thus the brightness temperature contrast between the two bands may be used to roughly estimate the detectable concentration based on a noise equivalent temperature of approximately 0.1 K. For other scenarios where the cloud vapor is not at the ambient-air temperature we must manually input an updated T_{gas} value. If such a value is not available then T_{gas} can be defined as one of the parameter to be retrieved through the minimization process. Several simulations have indicated that good T_{gas} retrievals can be obtained with high temperature cloud vapors and for chemicals having a wide spectral signatures.

τ_{near};... is defined as the spectral transmittance of the atmosphere (Fig. 1) between the cloud vapor and the sensor (Eq. 49). A good knowledge of this component is essential because there are many atmospheric lines that can interfere with the chemical vapor signature. Several parameters are required to accurately model this transmittance. The atmospheric transmission model implemented into GASEM is presented at the next section.

N_{near};... is defined as the near-field path radiance (Fig. 1) of the atmosphere from the cloud position to the sensor (Eq. 49). Again this term is important because of the atmospheric lines that can interfere with the chemical vapor signature. Details of the modeling are reported in the next section (Sec. 4.3).

ΔL^a_{clear} and ΔL^b_{clear},... are defined as the clear-scene radiance drifts associated with the background changes between the reference measurement, L'_{clear}, and the actual values, L'_{clear} and L''_{clear}. Equations 17a to 17d define these variables in relation with Fig. 3f. These clear-

scene radiance drifts are not known a-priori. In GASEM, they are included in the retrieval process as a first order correction. Algebraic details on this correction appear further (Sec. 4.4).

S_i;... is the measured raw spectrum (complex) associated with the differential detection (Eq. 52). It represents the co-addition of a variable number of individual scans. Actually, the instrument continuously co-adds the incoming spectra and periodically sends the current mean to the processing program. It is the primary measured input for GASEM.

K_2;... is the responsivity parameter, a measured input required for the radiometric calibration of the raw spectrum (Eq. 52). It has been defined and discussed in relation with Eq. 33.

re_2;... is the instrument residual parameter, also a measured input required for the radiometric calibration of the raw spectrum (Eq. 52). It has been defined and discussed in relation with Eq. 34.

B_s;... is the Planck radiance associated with the beamsplitter temperature (known input) as defined in relation with the Eq. 29.

4.3 Atmospheric Transmission and Emission Modeling

To generate the calculated radiance differential intervening in the minimization equation, two more terms need to be evaluated i.e., the atmospheric transmittance, τ_{atm}, and the atmospheric radiance, N_{atm}. In the initial phase of the GASEM development these terms were computed off-line with the MODTRAN model (Ref. 18) using meteorological inputs of temperature, humidity and ozone concentration. A limited success was obtained with this approach because the meteorological inputs were not always available or known with enough accuracy. To counter this limitation, a fast atmospheric transmission/emission model have been integrated into GASEM. This simplified model is a sort of look-up table version of the actual MODTRAN (version 3.7). The great advantage of this is that the modeling parameters for the atmosphere such as the temperature, the humidity and the ozone concentration can also be roughly adjusted, if required, through the minimization process.

In the fast model, the spectral transmittance of the atmosphere is defined as the product of three components i.e., the molecular transmittances of the dry air, τ_{nssr}^{dry}, the ozone transmittance, τ_{nssr}^{oz}, and the water vapor transmittance, τ_{nssr}^{H2O}:

$$\tau_{nssr} = \tau_{nssr}^{dry}(v,d)\cdot\tau_{nssr}^{oz}(v,d)\cdot\tau_{nssr}^{H2O}(v,H,d). \qquad [58]$$

Each component can have one to several lines or bands in the mid and far IR i.e., the spectral region for which the fast model is intended. It is important to note that the aerosol, cloud and rain components have been neglected in the current formulation. The dry-air component includes the contributions of all other active molecules in the infrared, namely CO_2, CO, N_2O, CH_4, O_2 and N_2 assuming mixing ratios consistent with the US standard conditions.

The transmittance of the dry-air component is given by

$$\tau_{nssr}^{dry}(v,d) = \exp\left[-\alpha_{dry}(v,d)\cdot\frac{p}{p_o}\cdot d\right], \qquad [59]$$

where α_{dry} is defined as an effective spectral absorption coefficient of the dry air, p is the ambient air pressure, p_o is a reference pressure (1013 mbar), and d is the distance between the cloud vapor and the receiver. The exponential transmittance formulation (Eq. 59) reduces to the Beer-Lambert law when the instrument can spectrally resolve each atmospheric lines i.e., a resolution of the order of 0.02 cm^{-1} at ground level. In this case, α_{dry} is rigorously independent of the propagation distance. For chemical detection purposes, the spectral resolution of the CATSI instrument is usually set at 4 cm^{-1}. At this resolution, the only way to satisfy the exponential formulation is by letting α_{dry} be a function of the propagation distance d. In the fast model, the current value of α_{dry}(d) at a distance d is numerically interpolated from a set of coefficients stored in the form of a look-up table (wavenumber vs distance). These coefficients have been evaluated from many runs done with the MODTRAN model at a resolution of 4 cm^{-1} and for different distances. The propagation distance, d, is the leading variable in Eq. 59. It can be either given by the user or fitted through the minimization process.

For the ozone component, the transmittance is defined by

$$\tau_{nssr}^{oz}(v,d) = \exp\left[-\alpha_{oz}(v)\cdot oz\cdot d\right], \qquad [60]$$

where α_{oz} is an effective spectral absorption coefficient and *oz* is the ozone concentration expressed in ppb (default is 30 ppb). In the case of ozone, we have found that a proper Beer-Lambert transmission modeling is achieved with an averaged α_{oz} that is approximately independent of *d*. This averaged α_{oz} used in GASEM has been derived from several MODTRAN runs (resolution of 4 cm^{-1}) done with different ozone concentrations and for different propagation distances. The ozone concentration, *oz*, can be either given by the user or fitted through the minimization process.

Of the three components, the transmittance of the water vapor is the most difficult to model. It is expressed as the product of two sub-components, i.e., the molecular lines transmission and the continuum transmission. It is defined by

$$\tau_{H2O}^{H2O}(\nu,d) = \exp\left[-\left(\alpha_{line}(\nu,Hd) + \alpha_{cont}(\nu)\right)\cdot H \cdot d\right], \qquad [61]$$

where α_{line} is an effective spectral absorption coefficient associated with the water vapor lines, α_{cont} is the spectral absorption coefficient of the water vapor continuum and H (g/m^3) is the absolute humidity. In this exponential formulation, $\alpha_{line}(Hd)$ depends on both the absolute humidity and the propagation distance. In the current model, the current value of $\alpha_{line}(Hd)$ is numerically interpolated from a set of coefficients stored in the form of a look-up table (absolute humidity times distance vs wavenumber). These coefficients have been evaluated from many runs done with MOTRAN at a resolution of 4 cm^{-1} and for different distance-humidity couples. For the continuum component, α_{cont} is evaluated analytically using the standard Clough, Kneizys and Davies formulation (Ref. 19). This is the formulation implicitly included in the MODTRAN model. The continuum implementation into GASEM is based on the equations and discussions appearing in a recent atmospheric transmission study (Ref. 20). The water vapor continuum is split into two parts referred to as the self-broadening (α_{cont}^{S}) and the foreign-broadening (α_{cont}^{F}) components such that

$$\alpha_{cont} = \alpha_{cont}^{S} + \alpha_{cont}^{F}, \qquad [62]$$

with

$$\alpha^{s}_{con} = H \cdot \nu \cdot \tanh\left(\frac{1.439\nu}{2T_{air}}\right) \cdot a \cdot C_s(\nu,296) \cdot \left[\frac{C_s(\nu,260)}{C_s(\nu,296)}\right]^{\left(\frac{296-T_{air}}{296-260}\right)}, \qquad [63]$$

and

$$\alpha^{r}_{con} = \nu \cdot \left(\frac{bP}{T_{air}} - aH\right) \cdot \tanh\left(\frac{1.439\nu}{2T_{air}}\right) \cdot C_r(\nu), \qquad [64]$$

where T_{air} and P are the temperature (K) and the pressure (mbar) of the ambient air, and $C_s(\nu,260)$, $C_s(\nu,296)$ and $C_r(\nu)$ represent the basic set of spectral broadening coefficients. These coefficients have been directly extracted from the MODTRAN model. The numerical values for the two constants are a = 4.516×10^{18} and b = 9.780×10^{20}. A brief but more complete discussion on the continuum, the associate coefficients and their units can be found in Ref. 20.

The fast transmission model discussed above does not contain any layering capability and is therefore restricted to horizontal and low-elevation angle scenarios. In these cases, the near-field radiance term, N_{near} can be accurately evaluated using simple expressions. In the current GASEM, the N_{near} calculations are restricted to these two specific scenarios. First, for the horizontal path scenario where the ambient temperature is assumed to be uniform and constant over the path, the near-field radiance is given by

$$N_{near} = (1 - \tau_{near}) \cdot B(T_{air}), \qquad [65]$$

where τ_{near} is the transmittance evaluated by Eq. 58, and B is the Plank radiance associated with the air temperature, T_{air}. Second, for low-elevation angle scenarios, the temperature is no longer constant over the path and the near-field radiance is approximately given by

$$N_{near} = (1 - \tau_{near}) \cdot B\left(\frac{T^{0}_{air} + T^{d}_{air}}{2}\right), \qquad [66]$$

where the effective temperature for the Plank emission term is taken as the average of the temperature at both end of the propagation path, i.e., at zero range near the receiver (T^{0}_{air}), and at range d near the cloud vapor (T^{d}_{air}).

In summary, in the fast atmospheric propagation model implemented into GASEM, the atmospheric transmittance and the atmospheric radiance are computed by Eqs. 58 and 66, respectively. A typical comparison of transmittances computed with GASEM (Version 2.11) and MODTRAN (Version 3.7) for a horizontal propagation path of 4 km is shown at Fig. 10a. The meteorological inputs used in both models correspond to a typical summer conditions with a humidity of 10 g/m^3, a temperature of 25 °C, a pressure of 1000 mbar and an ozone concentration of 60 ppb. As seen, the agreement is quite good over the far IR band. Typical differences are usually smaller than 1 % (absolute terms) with an exception near 1200-1250 cm^{-1} where a discrepancy of 2-5 % is observed. After investigation we have found that the water vapor continuum implementation into GASEM needs some minor refinements to remove this discrepancy. Fig. 10b shows the radiance comparison obtained for the same horizontal path scenario using the same meteorological inputs. Again the agreement is quite acceptable. Finally, the overall accuracy obtained with the fast atmospheric transmission/emission model implemented into the actual GASEM (Version 2.11) properly fulfills the operational requirements for a large class of horizontal and low-elevation angle scenarios. However, it is recommended to validate and scale the fast model accuracy with MODTRAN for slant-path scenarios involving temperature differences, $T_{air}^{d} - T_{air}^{0}$, greater than 15°-20° C, i. e. corresponding to difference in altitude of approximately 3 km.

4.4 Background Drifts Modeling

The last issue that remains to be addressed to complete the modeling aspect of the GASEM algorithm is related to the background drift terms appearing in the minimization equation (Eq. 54). This equation can be rewrite in a more convenient form such that

$$\min \sum_{\nu_{min}}^{\nu_{max}} \left(\left[\delta L^{*}_{calc} - \delta L^{*}_{meas} \right] + \Delta_{drift} \right)^2, \qquad [67]$$

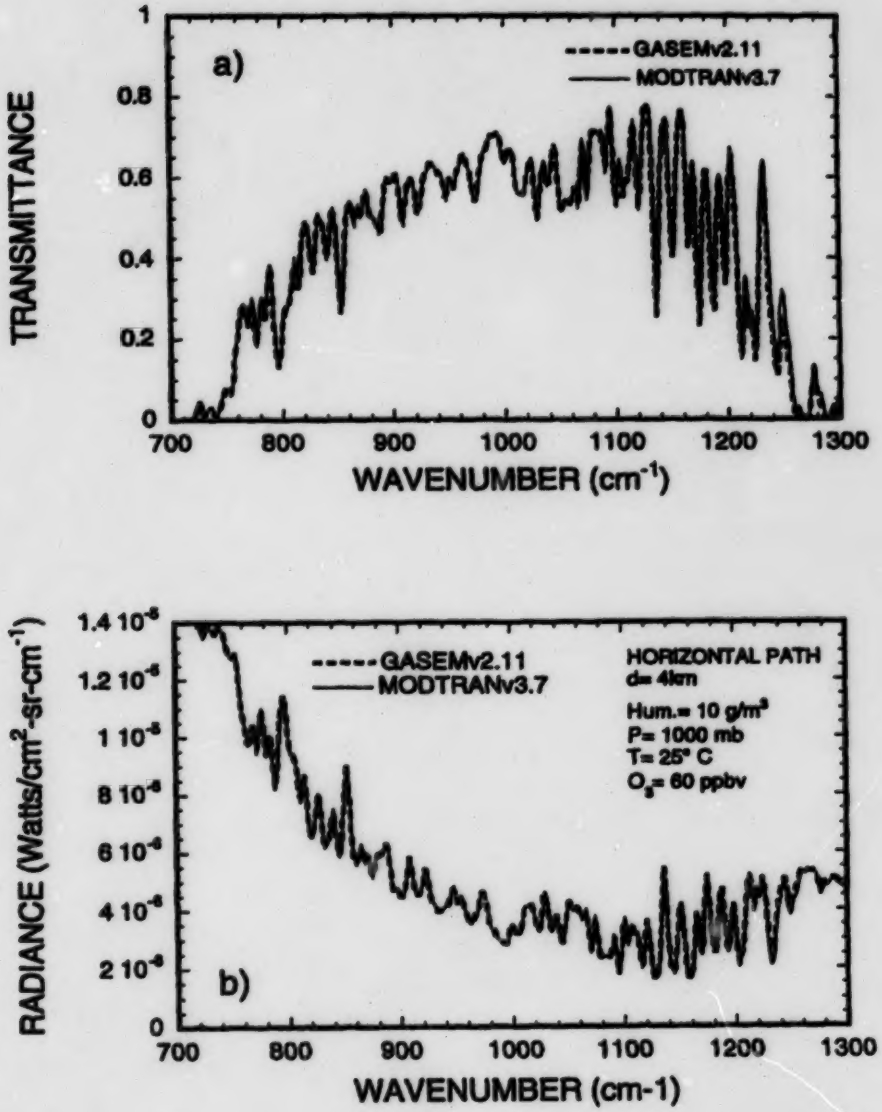

FIGURE 10 - Comparison between the built-in GASEM and the MODTRAN models for an horizontal path of 4 km; a) to transmittances and b) radiances

where the radiance drift term, Δ_{drift}, is defined, with reference to Eqs. 50, 53 and 54, by

$$\Delta_{drift} \equiv (\Delta_{calc} - \Delta_{meas}) = \left[f\left(\Delta L^a_{clear}(\tau_{gas} - 1) + \Delta L^b_{clear}\tau_{gas}\right) + \left(\frac{re_2}{L'_{clear} - B_s}\right)\Delta L^a_{clear} \right] . \quad [68]$$

This radiance drift, Δ_{drift}, takes into account, first the variation between the two backgrounds intervening in the differential measurement (ΔL^b_{clear}), and second the variation between the background of the clear-scene recording and the backgrounds of the differential measurement (ΔL^a_{clear}). These background variations (or drifts) have been discussed in relation with Eq. 17d and Fig. 3f.

For standoff detection experiments done in well controlled and stable environments it is often possible to obtain a background approximately uniform such that $\Delta L^a_{clear} \sim 0$ and $\Delta L^b_{clear} \sim 0$. This represents the ideal case. However, when the background scene is smoothly structured or for the detection from a moving platform (or a moving background), the radiance drift term (Δ_{drift}) can become significant. In these cases it must be taken into account by some means. Our approach to handle the background drifts and the corresponding Δ_{drift} is simply based on and limited by the GASEM capability to perform multi-parameter fits.

In a first attempt to estimate the radiance drift term (Δ_{drift}) it was empirically found that a linear function with wavenumber reproduces well the general tendency of many spectral observations. It is referred here as the linear offset approximation. An example of such an observation is shown in Fig. 6 where we can note the presence of an offset on the radiance differential curve. In this approximation, the radiance drift term is defined by the empirical function given by

$$\Delta_{drift} \equiv (a\nu + b) , \quad [69]$$

where , a and b represent the slope and the offset of the linear curve. In the current GASEM version (v 2.11) these are the two parameters that are adjusted through the SIMPLEX minimization process to take into account the overall effects of the background drift. In many cases, the inclusion of these two parameters is not only sufficient but also essential to ensure a proper retrieval of the chemical vapor concentration (CL).

In the next version of the GASEM algorithm, a more physical model for the background drift will be implemented. It is based on the following assumptions. First, the brightness temperature (θ_{Lclear}) associated with the recorded L^r_{clear} is computed using the inverted Planck expression i.e.,

$$\theta_{Lclear} = \frac{1.439\nu}{\ln\left(\frac{1.191\times10^{-12}\nu^3}{L^r_{clear}}+1\right)} \quad . \qquad [70]$$

This is equivalent to as defining an effective blackbody expression for L^r_{clear} such that

$$L_{clear} \equiv B(\theta_{Lclear}) = \left(\frac{1.191\times10^{-12}\nu^3}{e^{\left(\frac{1.439\nu}{\theta_{Lclear}}\right)}-1}\right) , \qquad [71]$$

and where the temperature becomes a spectral variables. Defining the two backgrounds drifts in terms of the brightness temperature yields

$$\Delta L^a_{clear} = B(\theta_{Lclear}+\Delta\theta_a) - B(\theta_{Lclear}) \qquad [72a]$$

and

$$\Delta L^b_{clear} = B(\theta_{Lclear}+\Delta\theta_b) - B(\theta_{Lclear}) \quad . \qquad [72b]$$

In this case, $\Delta\theta_a$ and $\Delta\theta_b$ are the two parameters to be fitted to take into account the two background drift terms. They are both expressed in Kelvin units. The main assumption behind this procedure is that the brightness temperatures of two arbitrary L_{clear} are connected by an additive constant independent of the wavenumber. It is referred to as the constant brightness temperature drifts approximation. This assumption is fairly consistent with observations done on several types of natural background such as trees, mountains, and clear and cloudy skies observed at low elevation angles.

Finally, it is reminded that the main objective pursued in this modeling effort has been to provide GASEM with all the necessary parameters required to support any horizontal and low-elevation angle scenarios. These modeling parameters take into account the

contributions from the intervening chemical cloud, atmosphere and background drifts. Several open-air experiments done to evaluate the current algorithm (GASEM Version 2.11) have shown good results that support the differential detection approach. However these experiments have also indicated that the method performances i.e., the detection probability and the false alarm rate would be mainly driven by the capability to handle the background drift component. GASEM Version 2.11 uses the linear offset approximation (Eq. 69) to handle the background drifts with two empirical parameter a and b. This approximation works well for a restricted class of smooth background variations. In the next version of GASEM, the background drift handling will be based on the brightness temperature approximation (Eq. 72) which should be more efficient to handle larger background variations. An important part of the future research efforts will be focussed on developing processing strategies for a better handling of the background drifts. That is a key issue for achieving an advanced processing algorithm for the differential detection of chemicals.

4.5 Correlation Factor

In the current GASEM algorithm, the detection and identification of a given chemical is achieved when the chemical cloud parameters retrieved through the SIMPLEX minimization are physically acceptable, and when a proper correlation factor between the measured spectrum and the spectrum calculated with the best fitted parameters is obtained. The correlation factor (r^2) is defined here as the square of the Pearson's correlation coefficient given by

$$r^2 = \frac{\left(\sum_{i=1}^{n_{chan}} (f_i - \bar{f})(y_i - \bar{y})\right)^2}{\sum_{i=1}^{n_{chan}} (f_i - \bar{f})^2 \cdot \sum_{i=1}^{n_{chan}} (y_i - \bar{y})^2} , \qquad [73]$$

with

$$f_i = \left(\delta L^*_{calc} + \Delta_{shift}\right) , \qquad [74]$$

and

$$y_i = \delta L^*_{meas} , \qquad [75]$$

P515096.PDF [Page: 55 of 86]

and where n_{chan} represents the number of spectral channels of the chosen band for the spectral fit, f_i is equal to the spectral radiance differential calculated with the best fitted parameters (Eq. 49) which also includes the radiance drift term due to the background variations (i.e. Eq. 68 approximated by Eq. 69), and y_i is equal to the measured spectral radiance differential (Eq. 52). The spectral average of the calculated and the measured radiance differentials are defined by $\bar{f}$ and $\bar{y}$, respectively. The sequence of operations performed in quasi real time by GASEM are, first to acquire and calibrate the measured spectrum, second to estimate the best fitted parameters using the SIMPLEX minimization, and third to compute the corresponding correlation factor (r^2). This factor, which varies from no-correlation (0) to perfect-correlation (1), is then used to make a decision on the presence or the absence of a given chemical clouds.

Usually, for very short acquisition times (few hundredths of a second for the CATSI instrument) the measured spectrum is dominated by a strong random noise component which totally masks the spectral features associated with the chemical cloud. In this case, the corresponding best fitted parameters have no physical meaning and the resulting r^2 is approximately zero. For longer acquisition time, the spectral noise is damped and the spectral features of the chemical cloud can become contrasted enough to declare a detection. In this case, the corresponding best fitted parameters are physically acceptable and the magnitude of the resulting r^2 should be consistent with the value expected from noise considerations. This expected value referred to as the noise limited correlation factor (r^2_{NL}) is estimated from the following considerations.

If we assume that the measured spectrum is hypothetically equal to the calculated spectrum with the addition of a spectral random noise component, N_i, then

$$y_i = f_i + N_i \ , \qquad [76]$$

with $\bar{N} \approx 0$ and $\bar{y} \approx \bar{f}$. The bar over the variables means the spectral average taken over the band used for the spectral fit. In this case, the correlation factor becomes

$$r_{NL}^2 = \frac{\left(\sum_{i=1}^{n_{chan}}(f_i - \bar{f})^2 + \sum_{i=1}^{n_{chan}}(f_i - \bar{f})N_i\right)^2}{\sum_{i=1}^{n_{chan}}(f_i - \bar{f})^2 \cdot \sum_{i=1}^{n_{chan}}(f_i + N_i - \bar{f})^2} \quad . \qquad [77]$$

An inspection of Eq. 77 indicates that the presence of the random noise component (N_i) in the second summation of the numerator makes this contribution significantly smaller than the first term. If we make the approximation that this second summation is always negligible then the noise limited correlation factor simplifies to

$$r_{NL}^2 = \frac{1}{1 + \dfrac{\sum_{i=1}^{n_{chan}} N_i^2}{\sum_{i=1}^{n_{chan}}(f_i - \bar{f})^2}} \quad . \qquad [78]$$

Moreover when the number of spectral channels n_{chan} is large enough to ensure an acceptable Gaussian statistics then the root mean square (RMS) of the spectral noise can be linked to the noise equivalent spectral radiance ($NESR$) by the following relation

$$\sqrt{\frac{1}{n_{chan}}\sum_{i=1}^{n_{chan}} N_i^2} \approx NESR \quad . \qquad [79]$$

Inserting this result into Eq. 78 yields, after simplification,

$$r_{NL}^2 = \frac{1}{1 + \dfrac{(NESR)^2}{[RMS(f)]^2 - [AVE(f)]^2}} \equiv \frac{1}{1 + \dfrac{VAR(noise)}{VAR(f)}} \quad , \qquad [80]$$

where the root mean square of f_i (the spectral radiance differential calculated with the best fitted parameters) is defined by

$$RMS(f) \equiv \sqrt{\frac{1}{n_{chan}}\sum_{i=1}^{n_{chan}} f_i^2} \quad , \qquad [81]$$

and the average of f is defined by

$$AVE(f) \equiv \sqrt{\frac{1}{n_{chan}} \sum_{i=1}^{n_{chan}} f_i} = \bar{f} \quad . \qquad [82]$$

In this form, Eq. 80 indicates that the noise limited correlation factor r_{NL}^2, is simply related to a variance ratio i.e, the variance of the noise, $VAR(noise)$ divided by the variance of the best fitted function $VAR(f)$.

The $NESR$ is a standard variable used to characterize the radiometric sensitivity of FTIR systems. It is defined by

$$NESR(t_a) = \frac{K_S}{\sqrt{t_a}} \quad . \qquad [83]$$

where t_a is the spectrum acquisition time and K_S is a system constant that includes several instrument parameters. The definition of K_S (see Flanigan, Ref. 9) is

$$K_S = \frac{\sqrt{A_d}}{D^* \cdot (A\Omega) \cdot \xi \cdot \delta\nu} \quad . \qquad [84]$$

where A_d and D^* represent the area and the detectivity of the detector, respectively, $A\Omega$ and ξ are the throughput and the transmission of the optical system, respectively, and $\delta\nu$ is the spectral resolution of the FTIR interferometer (usually 4 cm^{-1} for CATSI). Inserting Eq. 83 into Eq. 80 to obtain the time evolution of the noise limited correlation factor yields

$$r_{NL}^2(t_a) = \frac{1}{1 + \dfrac{\left[K_S^2/t_a\right]}{[RMS(f)]^2 - [AVE(f)]^2}} \quad . \qquad [85]$$

It is important to emphasize the interrelation between the two correlation factors defined at Eqs.73 and 85. In GASEM, the acquired spectrum at a given time, t_a, represents the current average done over the number of scans co-added since the beginning of the acquisition. The starting and the ending times of the acquisition are controlled by the

operator. It can vary from a fraction of a second to several minutes, depending on the radiometric contrast produced by the chemical cloud. Because the noise decreases as the square root of the time (Eq. 83), better detection conditions are achieved for longer acquisition time. In parallel with the spectral acquisition, the algorithm continuously process the incoming spectrum to generate the current correlation factor r^2(Eq. 73), to compute the best fitted parameters (by SIMPLEX minimization) and the best fitted spectrum (f), the resulting noise limited correlation factor r^2_{NL} (Eq. 85), and to display the result. As discussed above all these results obtained in quasi real-time can be used to make a decision on the presence or the absence of a given chemical cloud.

In the decision-making process, the noise limited correlation factor r^2_{NL} acts as an upper limit for the actual correlation factor r^2. For instance, if the best fitted parameters are physically acceptable and if $r^2 \approx r^2_{NL}$, then the spectral residual between the calculated and the measured spectra (f_i - y_i) is essentially dominated by the random noise. In this case, a detection can be declared. Fig. 11a shows an example of a strong match between r^2(.825) and r^2_{NL} (.900) obtained for the sounding of a vapor of methanol. The consistency between r^2 and r^2_{NL} indicates that the modeling parameters (cloud vapor, atmosphere and background drifts) adequately reproduce the experimental observations. However, there are cases where the best fitted parameters are physically plausible but with an r^2 too small compared with r^2_{NL}. This may have several causes such as a wrong choice for the expected chemical(s), the presence of unexpected interferents, and the inaccuracy of the modeling parameters (cloud vapor, atmosphere and background drifts). Fig. 11b shows an example of a weak match between r^2(.173) and r^2_{NL} (.884) obtained for the methanol vapor but when the expected chemical is wrongly chosen to be ethanol. In such cases, the spectral residual (f_i - y_i) exhibits systematic differences rather than random noise fluctuations. The inspection of the spectral residual helps find the anomaly and apply the required corrections.

4.6 Algorithm Functionalities and Examples of Operation

The GASEM software (v2.11) is coded in C-language and works under the DOS environment. The basic task of this software is to continuously co-add the spectra acquired with the CATSI instrument and to process on-line the current mean spectrum. The processing consists in adjusting, through the SIMPLEX minimization, a set of selected gas, atmospheric and background parameters to produce a calculated spectrum that best fits the spectral features of the measured spectrum. In principle any combinations of the modeling

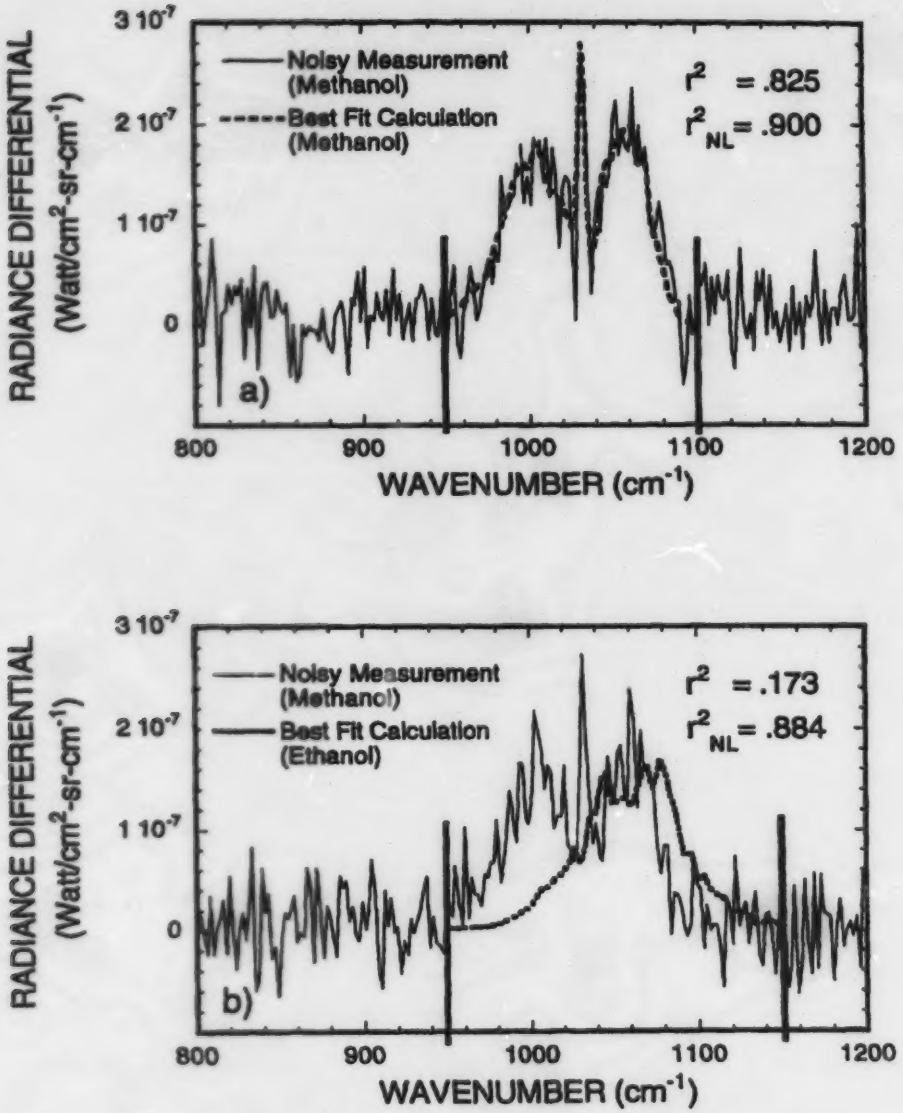

FIGURE 11 -Examples of the actual r^2 and the noise limited r^2_{NL} that correlate the measured and the best fit spectra: (a) the expected cloud vapor is properly chosen (i.e. methanol), and when (b) it is wrongly chosen (ethanol).

parameters defined in the previous sections can be adjusted through the fitting process. These parameters include, the *CL* and T_{gas} associated with the chemical cloud, the *H*, *oz* and *d* of the atmospheric propagation model and the two background drift parameters *a* and *b*. There is also a provision for monitoring chemical vapor mixtures composed of up to ten species for which each CLs can in principle be estimated. However, for most of the field experiments performed to date at short standoff detection ranges varying from 50 m to 600 m, the uses of two (*CL*, T_{gas}), three (*CL*, T_{gas}, *b*) or four (*CL*, T_{gas}, *b*, *a*) fitting parameters were adequate to properly monitor the chemical clouds.

To illustrate the monitoring capability of the software, Figure 12 shows two typical screen pictures generated with GASEM during an acquisition. This acquisition corresponds to the remote monitoring of an SF_6 release. Figures 12a and 12b display the screens obtained after 1 and 11.5 time-units (t.-u.) of monitoring, respectively. It is important to note that for the case reported in Fig. 12, one t.-u. corresponds to approximately 0.5 second. The screen is divided into several panels. The menu bar is used to select various functions of the software and to set various parameters. On the left side of the screen there are four panels: A plot of a selected parameter as a function of time (t.-u.) is displayed in every panel. The name of the variable being plotted appears on the top left corner and its current value appears on the right. The top left window displays the time evolution of the current r^2 and the noise limited r^2_{NL} correlation factors. Note that for this particular case, the r^2_{NL} calculation was not activated and an arbitrary value of one was continuously displayed by default. The "scale" variable displayed on the second panel from the top (left-hand side) has exactly the same meaning as the path-integrated concentration, *CL*. The third and the fourth panels on the left-hand side corresponds to the time evolution of the offset parameter (*b*) and the cloud vapor temperature (T_{gas}), respectively.

The "Spectrum" window at the top right of Fig. 12 is a plot of the acquired differential spectrum (y_i) together with the superimposed best fit spectrum (f_i). The fitted spectrum is bounded by the two vertical dashed lines that define the band chosen for the spectral fit. The horizontal axis is the wavenumber (cm^{-1}) and the vertical axis is in radiance units (Watts / cm^2-sr-cm^{-1}). The plot appearing in the "Residual" window is the difference between the measured and the calculated spectra. The parameter box below the residual window displays

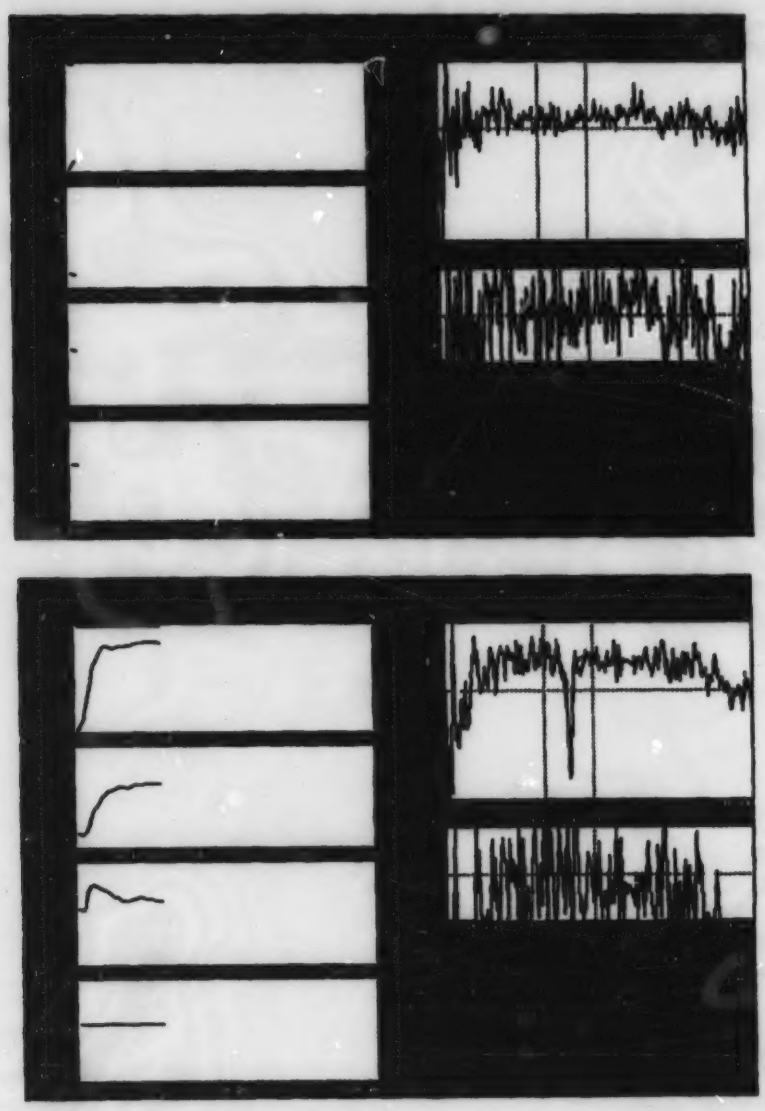

a)

b)

FIGURE 12 - Screen displays for the remote monitoring of an SF_6 release probed at a distance of 460 m: (a) after approximately 1 t.-u., and (b) after 11.5 t.-.u. The radiative contrast between the SF_6 vapor and the background is 1.4° C. The path-integrated concentration probed by the differential method varies from 0 to 19 ppm-m during the complete episode of release.

the information related to the acquisition and the fitting process. For instance after 11.5 t.-u. of SF_6 release (Fig. 12b) we have: 0 for the number of "Scans done" (not activated); 11.5 t.-u. for the "Time elapsed"; 171 "Simplex iterations" for the current fitting; 2 for the number of "Fit Parameters" (*CL* and *b*); "Brightness Tamb" of 301.4° K for the ambient air temperature deduced from L_{clear}; "Brightness Tback" of 302.8° K for the effective background temperature deduced from L_{clear}; a brightness temperature contrast "DeltaT" of 1.4° K; the number of intervening chemical species "N_{gas}" equal to 1; and the names of four output files generated by pressing the corresponding hot key. These hot keys are: "R" to produce a text file (*.TXT) of the time evolution of the various parameters generated during the acquisition, "D" to generate a text file (*.RWA) that includes the current measured and best fitted spectra, "S" to create a file of the current screen display (*.BMP), and "A" to generate a large binary file that contains the time evolution of the acquired and calculated spectra (*.SPA). This *.SPA file serves as input to GASEM to replay the full acquisition episode in a post-processing mode. Finally, the bottom window specifies the gas under study and the spectral band used for the fit.

In its current form, GASEM represents a quite useful and practical tool for the on-line remote monitoring of chemical vapors. To emphasize this point, it is convenient to document the SF_6 monitoring experiment introduced in Fig. 12. In this experiment, the CATSI instrument was located at a distance of 460 m (horizontal) from the SF_6 source position (tank). The flow rate of the SF_6 released from the tank and dissipated in the air was kept constant at a rate of approximately 20 l/m. The experiment was performed at DREV (Parc Lemay) in the afternoon of a nice summer day (14 Jul 99, 2:30 p.m.) with clear sky conditions, ambient temperature of 27.4° C, relative humidity of 46 %, high visibility (> 24 km), and south wind of approximately 10 km/hr. Fig. 12a represents a screen shot generated approximately 1 t.-u. (0.5 s) after the beginning of the release. As seen in the "spectrum" panel (top right), the measured spectral radiance differential exhibits a significant random noise content and a positive offset indicating the presence of a small background drift. The best fitted spectrum which smoothly overlap the measurement in the selected 890 and 1000 cm^{-1} window indicates a small signal-to-noise ratio with a correlation factor, r^2, of approximately 8% (top left panel). This small signal-to-noise ratio has three causes, i.e., the small amount of SF_6 that fills the sensor field of view at the beginning of the release (3.5 ppm-m), the weak temperature contrast between the vapor and the background scene (1.4° C), and the noise content for this relatively short time of acquisition. For comparison purposes, Fig. 12b represents a screen shot generated approximately 11.5 t.-u. (5.3 s) after the

beginning of the release. In this case the spectral fit appearing in the "Spectrum" panel reveals a quite good correlation factor (r^2) of 84%, and a *CL* of 19 ppm-m. In addition, the random noise that dominates the spectral residual shown in the "Residual" panel has decreases by approximately a factor of 3 which fits the square law dependence with the acquisition time. This experiment illustrates well the prime functionality of GASEM i.e., the on-line remote monitoring of chemical vapor parameters (*CL* and T_{gas}).

Another useful functionality included in GASEM is referred to as the search option. This search option is designed to perform an initial chemical identification prior to the monitoring operation. It consists of the repeated application of the SIMPLEX on a pre-recorded target spectrum to generate the best fit parameters for each of the chemicals included in a database of potential threats. Essentially this database contains the spectral absorption coefficients for all of the considered chemical threats. Fig. 13 gives an example of the search functionality applied to a spectrum of methanol measured in a recent field experiment. For this case, 18 chemicals were considered in the search database. The main result of this analysis appears in Fig. 13a where the diagram of correlation factors (r^2) versus chemicals clearly identifies the methanol as the actual chemical vapor with a r^2 = 85%. Fig. 13b shows a screen shot corresponding to the best fit obtained with the methanol. Because of its spectral similarity, the second closest score is attributed to GB with a correlation factor of approximately 29%. The normalized absorption coefficients (spectral signatures) of several chemicals that have a partial overlap with the spectral signature of methanol and used in the search database are plotted in Fig 14a. A second example of the search functionality applied to a vapor of ammonia is reported in Fig, 15. Again, the diagram of correlation factors versus chemicals clearly identifies the ammonia as the actual chemical vapor with a r^2 = 72%, and the two closest scores are attributed to octamethyl (17%) and chloroform (17%). The normalized absorption coefficients of chemicals that have a partial overlap with the spectral signature of ammonia and utilized in the search database are plotted in Fig 14b. Finally, Fig. 15b shows a screen shot corresponding to the best fit obtained with the ammonia.

In concluding this chapter it is convenient to summarize the progress achieved in the development of an algorithm (GASEM) adapted to the standoff detection of chemical vapors by differential FTIR radiometry. Firstly, a fast radiative transfer model that takes into account the contribution due to the chemical vapor, the atmospheric propagation and the background environment has been developed. Secondly, a SIMPLEX minimization capability has been implemented into the algorithm for the fast calculation of the detection parameters. Finally, a

specialized user interface that displays the current measured and best fitted spectra together with the time evolution of various detection parameters has been constructed. The primary functionality of the GASEM algorithm in its current form is the on-line remote monitoring of chemical vapor parameters (CL and T_{gaz}). This tool is also used to develop an optimized processing algorithm for the automatic standoff detection, identification and quantification of chemical vapors.

5.0 REMOTE MONITORING OF CHEMICAL VAPORS: RESULTS

To illustrate the capabilities of our passive remote monitoring method we have selected a data set recorded in a recent open-air experiment (Ft. Riley, Kansas, September 1998). DREV was involved with the Edgewood Research, Development and Engineering Center (ERDEC) in the collection of ground-based passive FTIR data for characterizing chemical vapors released from a well-controlled plume generator or stack (Ref. 21). Preliminary results obtained for four different compounds were qualitatively discussed in a preceding paper (Ref. 22). The current analysis focuses on the quantization results obtained for the methanol vapor, and shows examples of results obtained for a vapor of ammonia and for a binary mixture of ammonia-methanol.

5.1 Methanol Vapor Releases and Monitoring Conditions

The temperature of the stack was approximately constant at 200 °C, and for each release the flow rate was kept constant for approximately one half to one hour period. The on-line monitoring with GASEM was run to simultaneously retrieve the two chemical vapor parameters CL, T_{gaz} and the offset, b, that was used as a sole parameter for taking into account a possible background drift (the slope parameter a was not necessary). Other parameters required by the GASEM built-in atmospheric model such as the air temperature and humidity were obtained from on-site meteorological measurements while for ozone a default concentration of 30 ppmb was used. Meteorological conditions were ideal throughout the trial period with clear sky conditions, temperatures from 20 to 30 °C and humidities between 40 to 60 %. The spectral absorption coefficient (α_ν) which acts as an input "fingerprint" for GASEM was taken in the QASoft database (Infrared Analysis Inc., USA).

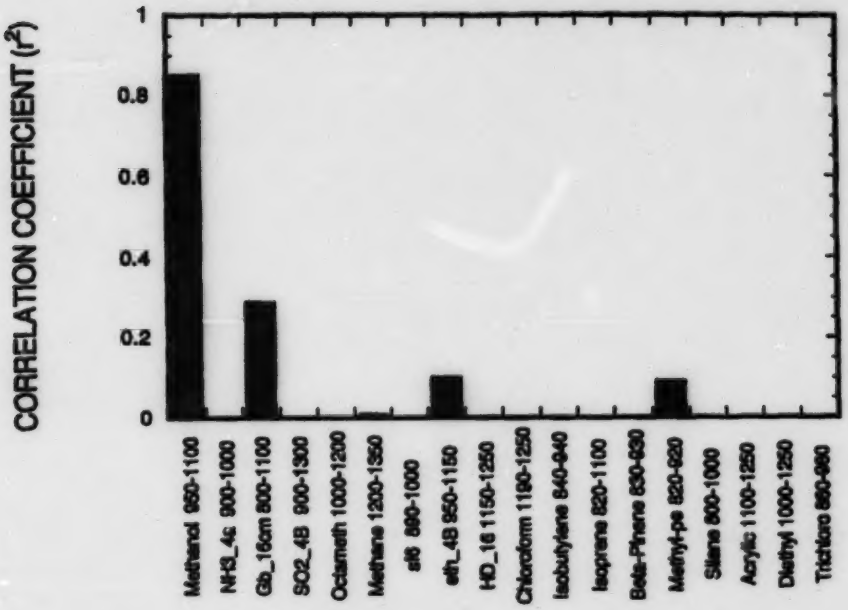

a)

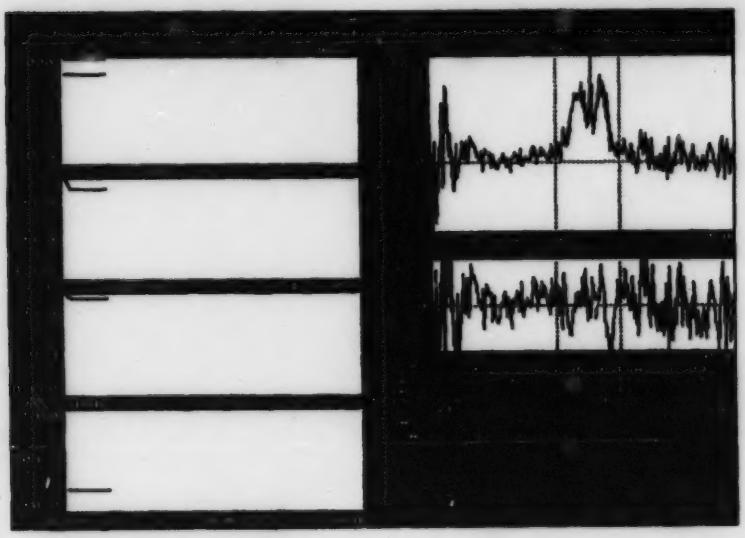

b)

FIGURE 13 - Example of the search functionality for methanol: (a) the correlation factors obtained for each of the 18 hypothetical chemicals and (b) the resulting spectral match for the highest r^2 scored with methanol.

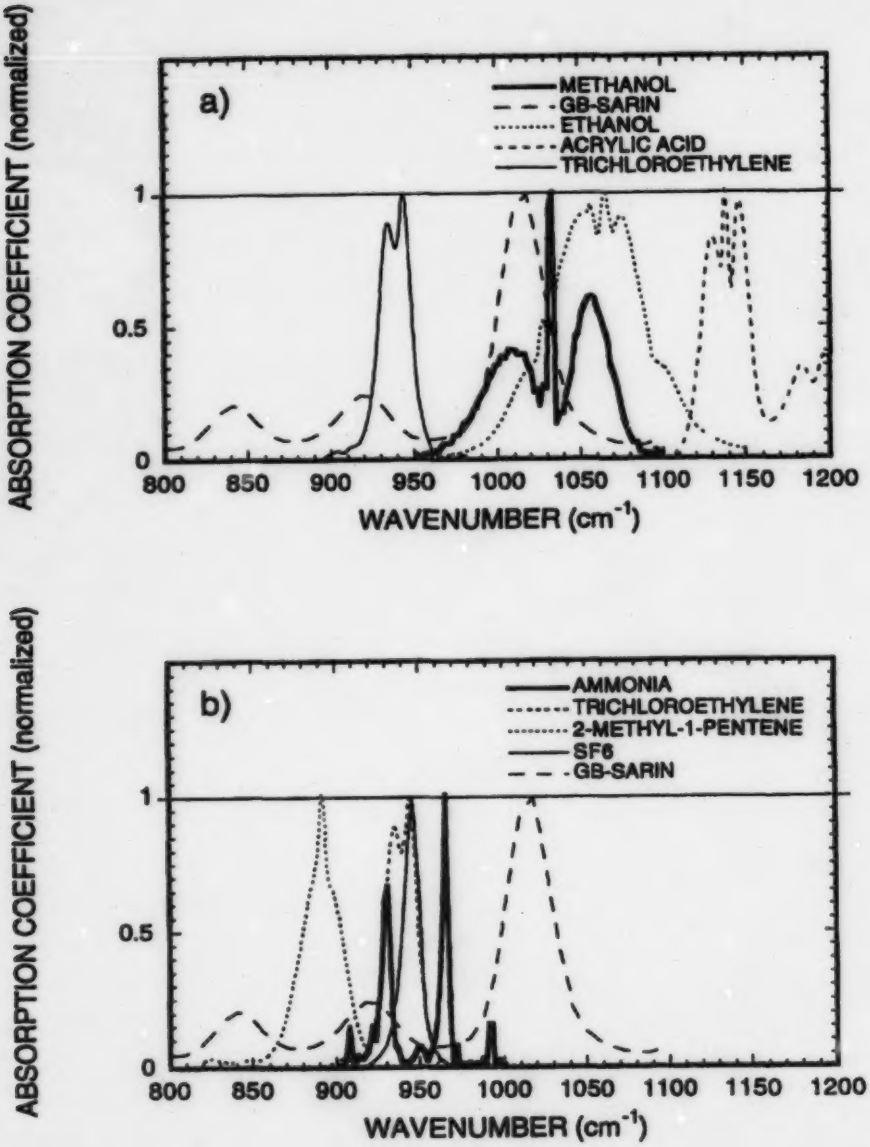

FIGURE 14 -Several examples of spectral signatures (normalized) that partially overlap the signature of methanol vapor (a) and of ammonia (b)

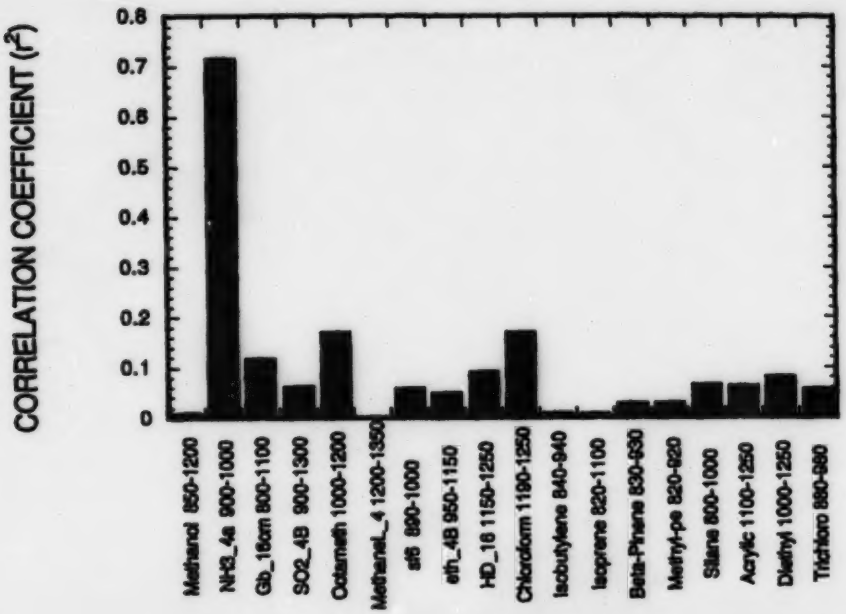

a)

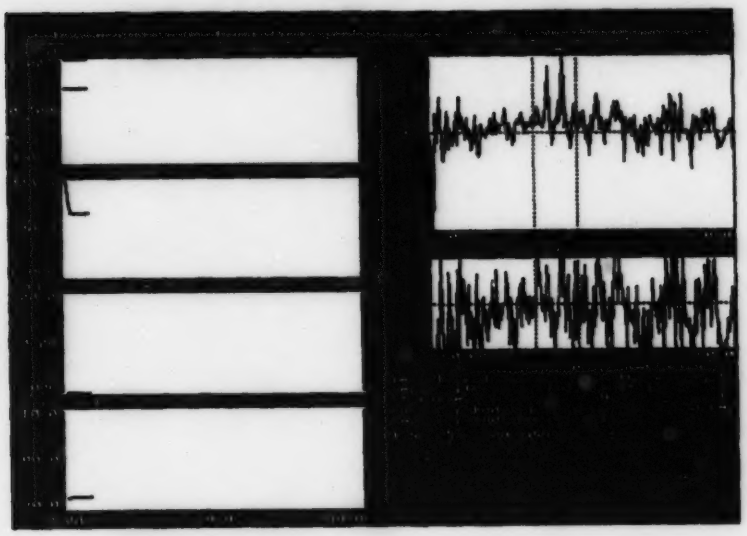

b)

FIGURE 15 - Example of the search functionality for ammonia: (a) correlation factors obtained for each of the 18 hypothetical chemicals and (b) the resulting spectral match for the highest r^2 scored with ammonia.

One purpose of the experiment was to monitor the concentration and the temperature of the methanol vapor at different locations across the plume. Figure 16 shows an example of plume monitoring for the seven locations probed with the CATSI system. A visible camera boresighted with the CATSI telescope is used to point at different parts of the plume. The circular field of view of the instrument with the inner crosshair is shown at location 1 (approximately 60 cm above the stack), while other sounded locations are marked by the corresponding number. These locations were chosen to maximize the plume signal at a given azimuth position. The distance plume-receiver was 105 m and the diameter of the stack was approximately 40 cm. Note that for each measurement the reference telescope-1 used for background subtraction was offset in azimuth by approximately 5.0° in the opposite direction of the plume (left side ; outside of the figure). Also seen in Fig. 3a is a large retro-reflector assembly (left of the cross-hair) that is part of an active FTIR transmissometer system used for the *CL* truthing at the outlet of the stack (Ref. 21).

Figures 17 to 19 summarize the monitoring procedure and calculations associated with locations 1, 4 and 7 of the plume, respectively. On each one, the measured spectrum (dotted line) which contains a certain amount of random noise is plotted for the spectral region extending from 700 cm^{-1} to 1300 cm^{-1}. The CATSI interferometer was operated at an apodized resolution of 4 cm^{-1} with a field of view of 7 mrad and a co-adding time of approximately one second. The GASEM processing consisted in adjusting the chemical vapor parameters to generate a calculated spectrum (δL_{calc}) that best fits the measured one (δL_{meas}) in the spectral band from 850 cm^{-1} to 1200 cm^{-1}. For each location, the correlation factor between the measured and the best fit spectra is given together with the retrieved gas temperature and concentration. For instance, for location 1 (Fig. 17) the correlation factor is r^2=0.98 and the resulting vapor parameters are T_{gas}= 335.6 K and CL=1933 ppm-m. For location 4 (Fig. 18) the correlation factor is r^2=0.70, T_{gas}= 295.7 K and CL=362 ppm-m. For location 7 (Fig. 19) the correlation factor is r^2=0.39, T_{gas}= 294.8 K and CL=245 ppm-m. The bottom curve on each graph represents the spectral residual.

As seen, the dominant random noise of the residual indicates that the radiative transfer modeling in GASEM is free of major systematic errors, except for location 1 (right above the stack outlet) where a spectral feature can be observed in the residual. This systematic feature arises from the fact that the temperature dependence of the absorption coefficient (α_ν) of the methanol vapor is not properly taken into account in our simplified plume model. Actually,

for this location right above the stack outlet, it has been found that the plume is generally well represented by a Gaussian profile with a high temperature at the center of the plume (approximately 180° C) and a rapid fall-off that reaches the ambient air temperature at approximately one stack diameter from the plume center.

In our simplified model the effective plume temperature is assumed to be uniform and the mean absorption coefficient corresponds to a specific temperature α_v. For the on-stack location 1, the best results were obtained with an α_v that corresponds to a temperature of approximately 125° C. However, this uniform plume temperature approximation with a mean α_v does not fully eliminate the systematic error apparent in the residual of Fig. 17. The plume modeling coupled with the temperature dependence of α_v temperature is a very important issue that impacts the quantization accuracy of chemical vapors near the stack outlet. A detailed description and validation analysis of the simplified plume model we have used for on-stack monitoring will be presented in a coming paper. For the off-stack locations where the chemical vapor is more uniformly spread with a lower effective temperature, satisfactory results were obtained with an α_v that corresponds closely to the ambient temperature (30° C).

5.2 Quantization Results for Methanol

Figure 20 summarizes the quantization results obtained for the overall methanol plume where the CLs, temperatures and correlation factors are plotted as functions of the locations in the plume. Note that for locations 4 to 7, two measurements were taken to evaluate the wind/turbulence induced variability. As seen, the plume temperature (Fig. 20b) is maximum right above the stack (336 K) and steadily decreases to an average value of 296 K for location 7 situated at a distance of 4 m (+2°) from the center of the stack. The ambient air temperature measured at the ground level was 294 K and the effective background (sky) temperature was approximately 291.5 K providing an intrinsic thermal contrast of 3.5 K. The fine structure of the plume temperature profile above the stack (location 1) is not spatially resolved because the field of view (FOV) of the instrument is larger than the plume size at this location. Consequently, the effective temperature derived with GASEM for location 1 represents a weighted average that depends on a the plume temperature profile (as discussed above). For other locations the plume size gradually increases with the distance from the stack. For instance, a vertical sweep near location 4 indicated that the effective

FIGURE 16: The seven locations across the methanol plume monitored with the passive CATSI system

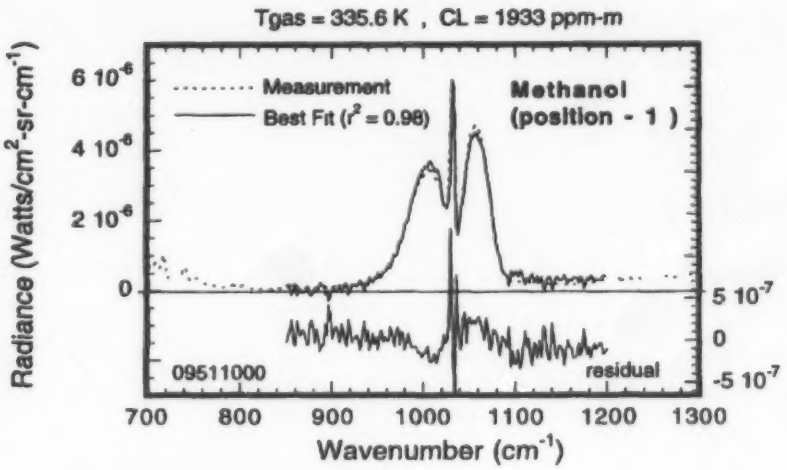

FIGURE 17 -The spectral fit obtained for location 1 on the methanol plume

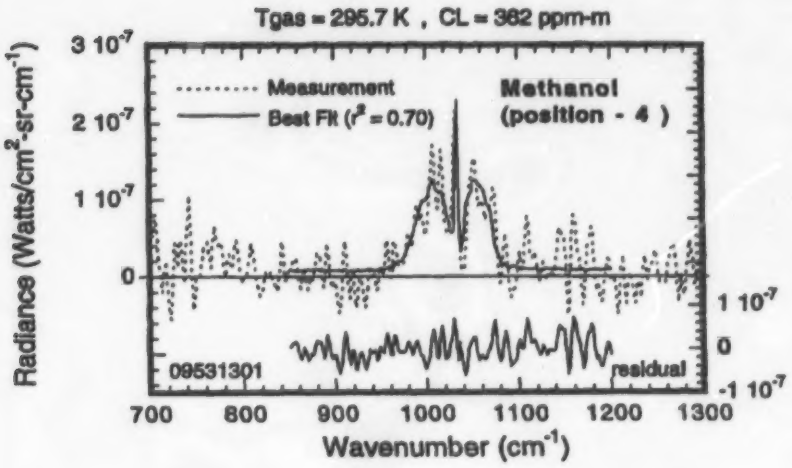

FIGURE 18 -The spectral fit obtained for location 4 on the methanol plume

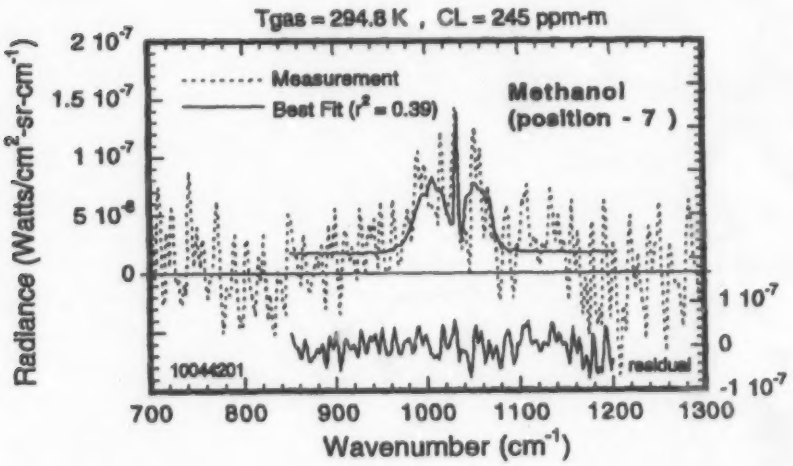

FIGURE 19 -The spectral fit obtained for position 7 on the methanol plume

angular size of the plume was approximately three times the FOV. In this case the temperature derived with GASEM should reflect the actual plume temperature. A consistent decreasing trend is observed for the integrated-concentration CL, from a maximum concentration of approximately 1950 ppm-m above the stack to an average value of 400 ppm-m for location 7. The observed structure of the plume agrees quite well with the expected effects caused by natural diffusion which tends to mix the ambient air with the chemical vapor reaching thermodynamic equilibrium away from the stack. The high correlation factors (Fig. 20c) obtained for most of the measurements indicate a good signal to noise ratio.

The vertical bars appearing on selected CL and T_{gas} results (Figs. 20a-b) represent the experimental errors. These errors were estimated based on GASEM simulations done with a random spectral noise content consistent with that observed in the measured spectrum. The only ground-truth data we have for this monitoring sequence corresponds to location 1. It is reported in Fig. 20a. In this case, the integrated-path concentration directly measured with the active FTIR transmissometer is CL=1350 ppm-m which is lower than the GASEM retrieved value of CL=1950 ppm-m. There are at least two explanations for this discrepancy. First, the high level of concentration and temperature inhomogeneity in the FOV of the instrument (location 1) can bias the mean solution found with GASEM; simulations based on a more accurate plume radiance model would clarify this point. Second, because of practical constraints, there was no attempt at systematically boresighting the active FTIR transmissometer (ground-truth) and the passive CATSI system with the consequence that each instrument probably looked at a slightly different portion of the plume. For this reason it is probably premature to definitely estimate the absolute accuracy of our approach; more validation analysis (coming paper) and experiments have to be done. However at this stage we can safely assert that the uncertainty on the methanol CL is roughly 30 % for on-stack measurements (location 1) while for off-stack measurements (locations 2-7) error calculations indicate a 15 to 30 % uncertainty on the CLs and a 2 to 5° on T_{gas}.

Monitoring done for the methanol plume at a greater range of 580 m also indicates a good consistency. Figure 21a shows the three locations probed with the CATSI system. At this distance (580 m), the field of view of the instrument is represented by a circle of approximately 4 meters in diameter. The stack which is hardly seen on the picture is just below the circle almost in line with the vertical axis of the crosshair. The fine structure of the

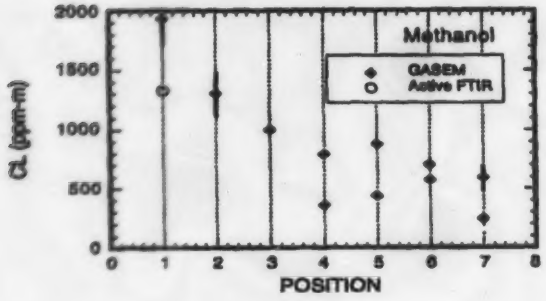

a)

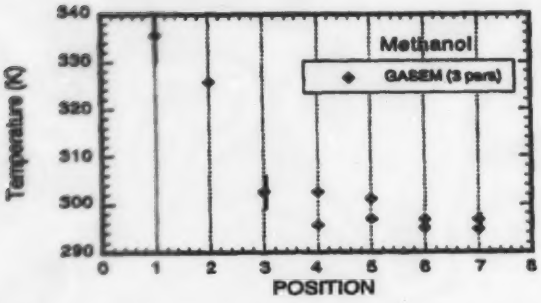

b)

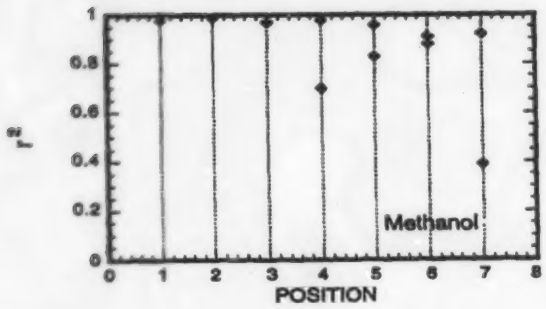

c)

FIGURE 20 - From top to bottom: (a) CLs, (b) temperatures and (c) correlation factors obtained by passive spectral radiometry with the GASEM algorithm for seven locations across the methanol plume

plume temperature profile above the stack (location 1) is not spatially resolved because the field of view (FOV) of the instrument is very much larger than the plume size at this range. Figure 21b summarizes the quantization results obtained for the three locations. Figure 22 shows the spectral fits and calculations associated with locations 1 and 3 in the plume, respectively. Note that for this case there was no truthing measurements available. Again, the correlation factors are quite high for the three locations, and a consistent downward trend is observed for the CLs, from a maximum concentration of approximately 1740 ppm-m right above the stack (location 1) to an average value of 824 ppm-m for location 3. The relatively small fitted temperature (301 to 303 K) is due to the averaging effect over the wide field-of-view that probes a large portion of the cooled vapor away from the stack axis.

5.3. Ammonia and Mixtures of Ammonia-Methanol

Several other compounds and binary mixtures have been monitored in conditions similar to those reported above for methanol, i.e. meteorological conditions, probing distance (105 m), instrument resolution (4 cm^{-1}) and acquisition time (1 sec.). A typical result obtained for ammonia is reported in Fig. 23. It corresponds to an off-stack location for which the GASEM calculation indicates a CL=258 ppm-m, a T_{gas}=296.9 K and a correlation factor of r^2=0.59. Although there was no truthing data available for validation of the off-stack ammonia measurements, a good consistency between results obtains at different locations was also observed for ammonia. However, as for the methanol vapor, the interpretation of on-stack measurements of ammonia is complicated by the high degree of plume inhomogeneity near the stack outlet and by the temperature dependence of the absorption coefficient of ammonia. A last example that illustrates the method capabilities for the remote monitoring of binary mixtures (ammonia-methanol) is reported in Fig. 24. This corresponds to an on-stack measurement done in conditions similar to those for methanol. As seen, the GASEM calculation indicates a high level of correlation r^2=0.963, a CL=130 ppm-m for ammonia and a CL=461 ppm-m for methanol assuming a fixed temperature of T_{MIX}=342 K for the vapor mixture. More validation results will appear in a coming report.

6.0 SUMMARY AND CONCLUSION

In this report, a novel approach for the passive standoff detection, identification and monitoring of chemical vapors is proposed. The originality of the method, which is referred to as the differential detection method, lies on the use of a double-input beam FTIR

a)

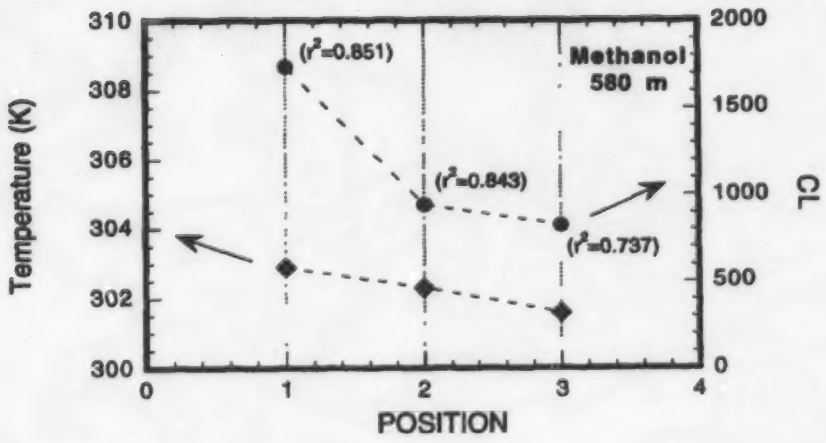

b)

FIGURE 21 - The three locations (a) across the methanol plume monitored with the passive CATSI system at a distance of 580 m, and (b) the resulting temperatures, CLs and correlation coefficients generated with the GASEM algorithm.

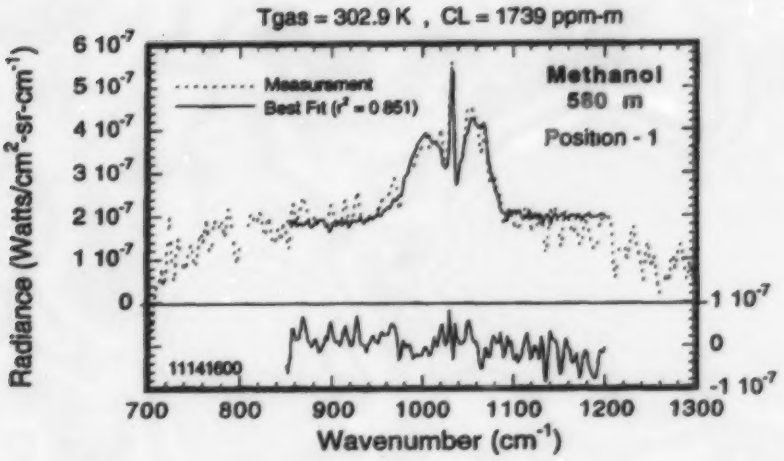

a)

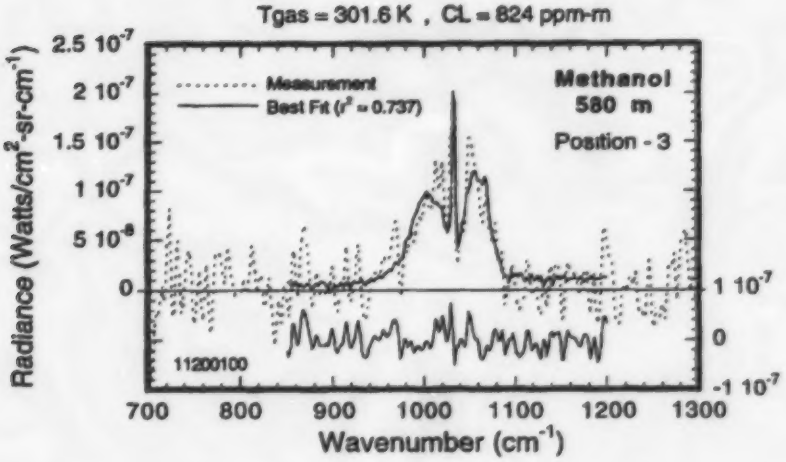

b)

FIGURE 22 - The spectral fit obtained for locations 1 (a) and 3 (b) of the methanol vapor plume located at a distance of 580 m from the CATSI receiver

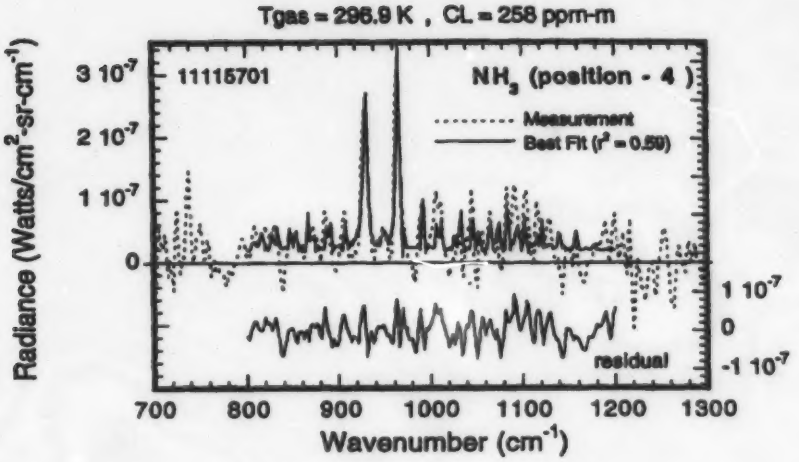

FIGURE 23 - The spectral fit and parameter calculations obtained for a vapor plume of ammonia located at a distance of 105 m from the CATSI receiver

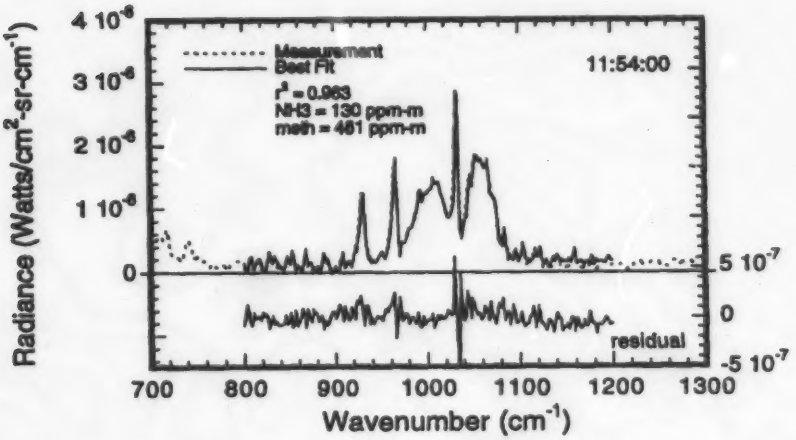

FIGURE 24 - The spectral fit and parameter calculations obtained for a vapor mixture of ammonia-methanol located at a distance of 105 m from the CATSI receiver

interferometer system (CATSI) optimized for optical subtraction. With this system, one input points at the background-scene and the other at the target-scene with the result that the two probed scenes are optically combined and subtracted in real time. This yields a cloud vapor spectrum minimally perturbed by the background radiation.

This report gives a full description of the differential detection method. To support its implementation, a radiative transfer theory has been formulated for the general case of slant path scenarios containing any type of background scenes. A first order correction takes into account a possible background inconsistency between the two probed scenes. A general procedure of radiometric calibration adapted for differential detection with a double-input beam FTIR interferometer has been developed and tested. This development has highlighted several attributes that make the differential detection method particularly efficient to handle the experimental constraints associated with scenarios of low target-to-background ratio. To explore and exploit the attributes of this method a processing algorithm called GASEM (Gaseous Emission Monitoring) has been developed. GASEM is not an advanced algorithm for automatic detection and identification. Rather, it represents a step-gap prototype that should lead to the construction of an advanced version. In its actual form, GASEM is built to control the interferometer acquisition, and to perform the on-line fitting that yields the integrated-concentration of the chemical target vapor.

It is well recognized that the remote quantization of chemical vapors by passive FTIR monitoring is a very challenging technique that has not been fully mastered yet. The differential detection method we propose appears promising. Perhaps, the greatest advantage of our approach is to provide, in the field, a spectrally clean signature of the remote chemical plume which facilitates its processing in real time. The results obtained to date with the GASEM algorithm for on-line detection and quantization are encouraging. The differential method has been successfully used to monitor several compounds and binary-mixtures. In particular, it has been utilized to map the integrated concentration and the temperature of a plume of methanol vapor. The uncertainties on the methanol plume monitoring have been estimated to be of the order of 15-30% for the integrated concentration, and 2 to 5° for the temperature. The consistency of the temperature and concentration solutions obtained for the methanol vapor also demonstrates the capabilities of GASEM and the relevance of the differential detection approach. Follow-on research activities will be directed towards improving the plume radiance model, addressing the temperature dependence of the chemical

absorption coefficients, refining the error calculation method, and pursuing the experimental validation, especially the capability to handle the atmosphere and other interferents.

7.0 ACKNOWLEDGMENTS

The author would like to thank Luc Bissonnette for many helpful suggestions related to this work. The expert technical assistance of Claude Bradette throughout this work is gratefully acknowledged. Special thanks go to Robert Kroutil and Roger Combs from the U.S. Army ERDEC for inviting us and for their collaboration throughout the Ft. Riley Experiment. We also thank Louis Moreau and Richard Lachance from ABB Bomem for their contribution in building the GASEM algorithm, and Charles T. Chaffin and Timothy L. Marshall from AeroSurvey Inc. for providing us with the ground-truth data.

8.0 REFERENCES

1. Kroutil, R. T., Ditillo, J. T., Small, G. W., " Signal Processing Techniques for Remote Infrared Chemical Sensing ", in Computer Enhanced Analytical Spectroscopy, H. L. C. Meuzelarr, Ed. (Plenum, New York, 1990). Vol. 2, pp. 71-111 (1990).

2. Hayden, A., Niple, E., and Boyce, B., " Determination of Trace-gas Amounts in Plumes by the use of Orthogonal Digital Filtering of Thermal-emission Spectra ", Appl. Opt., vol. 35, 2802, 1996.

3. Bennett, C. L., Carter, M. R., Fields, D. J. and Lee, F. D., " Infrared Hyperspectral Imaging Results from Vapor Plume Experiments ", Proceedings of the SPIE Conference, SPIE Vol. 2480, 274, 1995.

4. Thériault, J.-M., " IR Fourier Spectrometer for Differential Detection: Design, Prototype and Results ", DREV R- 9804, June 1998, UNCLASSIFIED

5. Thériault, J.-M., " Modeling the Responsivity and Self-Emission of a Double-Beam Fourier-Transform Infrared Interferometer ", Appl. Opt., Vol. 38, 505, 1999.

6. Revercomb, H. E., Buijs, H., Howell, H. B., Laporte, D. D., Smith, W. L. and Sromovsky, L. A., " Calibration of IR Fourier Transform Spectrometers: Solution to a Problem with the High-Resolution Interferometer Sounder " Appl. Opt., Vol. 27, 3210, 1988.

7. Kroutil, R. T., Combs, R. J., Knapp, R. B. and Godfrey, J. P., " Infrared Interferogram Analysis for Ammonia Detection with Passive FT-IR spectrometry ", Proceedings of the SPIE Conference on Electro-optical Technology for Remote Chemical Detection and Identification, Orlando 1996, SPIE Vol. 2763, 86, 1996.

8. Small, G. W., Carpenter, S. E., Kaltenbach, T. F. and Kroutil, T. F., " Discriminant Analysis Techniques for the Identification of Atmospheric pollutants from passive Fourier Transform infrared interferograms ", Analytica Chemica Acta Vol. 246, pp. 85-102 (1991).

9. Flanigan, D. S., " Prediction of the Limits of Detection of Hazardous vapors by Passive Infrared with the use of MODTRAN", Appl. Opt., vol. 35, 6090, 1996.

10. Flanigan, D. S., " Hazardous Cloud Imaging: A New Way of Using Passive Infrared", Appl. Opt., vol. 36, 7027, 1997.

11. Gruber, T., Grim, L., Berends, J. Jr., Pugh, M., and Thorpe, R., " An Aircraft Integration Solution for the COTS Standoff Chemical Sensor ", Proceedings of the SPIE Conference on Air Monitoring and Detection of Chemical and Biological Agents", Boston 1998, SPIE Vol. 3533, 128, 1998.

12. Polak, M. L., Hall, J. L. and Herr, K. C., " Passive Fourier-transform Infrared Spectroscopy of Chemical Plumes: An Algorithm for Quantitative Interpretation and Real-time Background Removal ", Appl. Opt., vol. 34, 5406, 1995.

13. " GASEM: User Manual for GASEM v2.07 ", DREV contract w7701-8-3615, BOMEM publication No. SP-BOM-004/98, (1998).

14. " GASEM: Detection of Hazardeous Gases by Remote Sensing ", DREV contract w7701-6-1087, BOMEM publication No. SP-BOM-001/97, (1998).

15. Press, W. H., Flannery, B. P., Teukolsky, S. A. and Vetterling, W. T., " Numerical Recipes: The Art of Scientific Computing ", Cambridge University Press, Secon Edition (1989).

16. Nedeler, J. A. and Mead, R., " A Simple Method for Function Minimization ", Computer Journal, Vol. 7, 308 (1965) May 1984, pp.340-362.

17. Caceci, M. S. and Cacheris, W. P., " Fitting Curves to data: The Simplex Algorithm is the Answer ", Byte Magazine, May 1984, pp.340-362.

18. Berk, A., Bernstein, L. S. and Robertson, D. C., " MODTRAN: A Moderate Resolution Model for Lowtran 7 ", Geophysics Laboratory, Hanscom Air Force Base, Mass., GL-TR-89-0122, 1989.

19. Clough, S. A., Kneizys, F. X. and Davies, E. W., " Line Shape and the water vapor continuum ", Atmos. Res. Vol. 23, 229, 1989.

20. Thériault, J.-M., Roney, P. L., St-Germain, D., Revercomb, H. E., Knuteson, R. O. and Smith, W. L., " Analysis of the FASCODE Model and its H_2O continuum based on Long-Path Atmospheric Transmission Measurements in the 4.5-11.5 μm Region", Appl. Opt., Vol. 33, 323, 1994.

21. Chaffin, C. T. Jr. and Marshall, T. L., " Generating Well-Characterized Chemical Plumes for Remote Sensing Research ", in Electro-optical Technology for Remote Chemical Detection and Identification III, Mahmoud Fallahi, Ellen Howden, Editors, Proc. SPIE Vol. 3383, 113-123 (1998).

22. Thériault, J.-M., Bradette, C., Lachance, R. L., Lafond, C., Moreau L., and Villemaire, A., "Interferometer and Algorithm for Differential Detection", Proceedings of the *Fourth* Workshop on Standoff Detection for Chemical and Biological Defense, Williamsburg VA, 26-30 Oct. 1998, Vol. 4, pp. 369-381, 1998.

UNCLASSIFIED

INTERNAL DISTRIBUTION

DREV TR-2000-156

1 - Director General
1 - Deputy Director General
1 - Chief Scientist
6 - Document Library
1 - J.-M. Thériault (author)
1 - G. Otis
1 - J.-M Garneau
1 - C. Carrier
1 - L. Bissonnette
1 - G. Fournier
1 - T. Smithson
1 - V. Larochelle
1 - D. Dion
1 - P. Chevrette
1 - J. Cruickshank
1 - P. Mathieu
1 - G. Roy
1 - J.-R. Simard
1 - J.-P. Ardouin
1- D. St-Germain
1 - C. Bradette

1- Dr. Andy Bell
Defence Evaluation and Research Agency
CBD Porton Down
Salisbury Wilts SP4 0JQ
UK

1 - Dr. T. Jones
U.S. Army Night Vision & Electro-optics
Laboratory
DELNV-VI
Fort Belvoir, VA 22060
U.S.A.

1 - Mr. R.K. Redfield
Department of the Army
Cold Regions Research & Engineering
Laboratory
Corps of Engineers
Hanover, NH 03755
U.S.A.

1 - Mr. A.P. Junchat
CELAR-Centre d'électronique d'armement
Division ASRE
35170 Bruz
France

1 - Dr. A. Kohnle
Forschungsinstitut für Optik (FfO)
Schloss Kressbach
74 Tübingen
Federal Republic of Germany

1- Dr. G. de Leeuw
Physics Laboratory FEL-TNO
Oude Wallsdorperweg 63
2597 AK, The Hague
Netherlands

EXTERNAL DISTRIBUTION

DREV TR-2000-156

1 - DRDKIM
1 - DRDKIM (unbound copy)
1 - DRDG
1 - DREA
1 - DREO
1 - DRES
1 - DCIEM
1 - DSTCCIS
1 - DSTL
1 - DST Pol
1 - DSTM
1 - DSTHP

2 - Drs. Joan Armour & Thor Jacobson
Defence Research Establishment Suffield (DRES)
PO Box 4000, Stn Main
Medecine Hat, Alberta T1A 8K6
CANADA

1 - Dr. Ngai Wong
US Air Force
AF Liaison ERDEC
AMSCB-AL
Aberdeen Proving Ground, MD 21010
U.S.A.

1 - Dr. James O. Jensen
U.S. Army SBCCOM
ATTN: SCBRD-RTE
Building E3549, Room C236
Aberdeen Proving Ground, MD 21010-5423
U.S.A.

2 - Ms. G. P. Anderson & Dr. A. Ratkowski
Phillips Laboratory
Geophysics Directorate (PL / GPOA)
Hanscom AFB
MA 01731
U.S.A.

1 - Dr. Ralph Leslie
Aeronautical and Maritime Research Laboratory
DSTO Melbourne
PO Box 4331
Melbourne VIC 3001
AUSTRALIA

UNCLASSIFIED
SECURITY CLASSIFICATION OF FORM
(Highest Classification of Title, Abstract, Keywords)

DOCUMENT CONTROL DATA

1. ORIGINATOR (name and address) Defence Research Establishment Valcartier 2459 Pie XI Blvd, North Val-Bélair, Québec G3J 1X5	2. SECURITY CLASSIFICATION (Including special warning terms if applicable) UNCLASSIFIED

3. TITLE (its classification should be indicated by the appropriate abbreviation (S, C, R or U)
Passive Standoff Detection of Chemical Vapors by Differential FTIR Radiometry

4. AUTHORS (Last name, first name, middle initial. If military, show rank, e.g. Doe, Maj. John E.)
Jean-Marc Thériault

5. DATE OF PUBLICATION (month and year)	6a. NO. OF PAGES	6b .NO. OF REFERENCES
January 2001		

7. DESCRIPTIVE NOTES (the category of the document, e.g. technical report, technical note or memorandum. Give the inclusive dates when a specific reporting period is covered.)
Technical Report

8. SPONSORING ACTIVITY (name and address)

9a. PROJECT OR GRANT NO. (Please specify whether project or grant)	9b. CONTRACT NO.
2EM10	

10a. ORIGINATOR'S DOCUMENT NUMBER	10b OTHER DOCUMENT NOS
	N/A

11. DOCUMENT AVAILABILITY (any limitations on further dissemination of the document, other than those imposed by security classification)

- [x] Unlimited distribution
- [ ] Restricted to contractors in approved countries (specify)
- [ ] Restricted to Canadian contractors (with need-to-know)
- [ ] Restricted to Government (with need-to-know)
- [ ] Restricted to Defense departments
- [ ] Others

12. DOCUMENT ANNOUNCEMENT (any limitation to the bibliographic announcement of this document. This will normally correspond to the Document Availability (11). However, where further distribution (beyond the audience specified in 11) is possible, a wider announcement audience may be selected.)
Unlimited

UNCLASSIFIED
SECURITY CLASSIFICATION OF FORM
(Highest Classification of Title, Abstract, Keywords)

UNCLASSIFIED
SECURITY CLASSIFICATION OF FORM
(Highest Classification of Title, Abstract, Keywords)

13. ABSTRACT (a brief and factual summary of the document. It may also appear elsewhere in the body of the document itself. It is highly desirable that the abstract of classified documents be unclassified. Each paragraph of the abstract shall begin with an indication of the security classification of the information in the paragraph (unless the document itself is unclassified) represented as (S), (C), (R), or (U). It is not necessary to include here abstracts in both official languages unless the text is bilingual).

This report presents a novel method for the passive standoff detection of chemical vapors by differential Fourier Transform Infrared (FTIR) radiometry. The originality of the method lies on the use of a double-input beam FTIR interferometer optimized for optical subtraction. For implementing this method, a radiative transfer model is formulated for the general case of slant path scenarios containing any type of background scenes. A procedure of radiometric calibration adapted for differential detection with a double-input beam FTIR interferometer is developed. A detection algorithm (GASEM) that controls the interferometer data acquisition and performs the on-line monitoring of chemical vapor parameters is described and validated. The differential detection method has been successfully tested in the field on several chemical vapors. In particular, it has been used to map the integrated concentration and the temperature of a plume of methanol vapor. In this case, the uncertainties on the methanol plume measurements have been estimated to be of the order of 15 to 30% for concentration, and 2 to 5° for temperature which represents an acceptable result for this type of passive sensing.

14. KEYWORDS, DESCRIPTORS or IDENTIFIERS (technically meaningful terms or short phrases that characterize a document and could be helpful in cataloguing the document. They should be selected so that no security classification is required. Identifiers, such as equipment model designation, trade name, military project code name, geographic location may also be included. If possible keywords should be selected from a published thesaurus, e.g. Thesaurus of Engineering and Scientific Terms (TEST) and that thesaurus-identified. If it is not possible to select indexing terms which are Unclassified, the classification of each should be indicated as with the title.)

Passive Standoff Detection

#515096

Chemical Vapor Monitoring

FTIR Spectrometer

Differential Detection

Double Beam Interferometer

UNCLASSIFIED
SECURITY CLASSIFICATION OF FORM
(Highest Classification of Title, Abstract, Keywords)